

Single-cell and spatial transcriptome analyses reveal tumor heterogeneity and immune remodeling involved in pituitary neuroendocrine tumor progression

Received: 10 October 2024

Accepted: 12 May 2025

Published online: 30 May 2025



Wan Su^{1,10}, Zhang Ye^{2,10}, Jifang Liu^{2,10}, Kan Deng², Jinghua Liu¹, Huijuan Zhu¹, Lian Duan¹, Chen Shi¹, Linjie Wang¹, Yuxing Zhao¹, Fengying Gong¹, Yi Zhang², Bo Hou³, Hui You³, Feng Feng³, Qing Ling⁴, Yu Xiao⁴, Yongdong Guo⁵, Wenyi Fan^{6,7}, Sumei Zhang⁸, Zixin Zhang⁸, Xiaomin Hu⁹✉, Yong Yao²✉, Chunhong Zheng^{6,7}✉ & Lin Lu¹✉

Pituitary neuroendocrine tumors (PitNETs) can be invasive or aggressive, yet the mechanisms behind these behaviors remain poorly understood, impeding treatment advancements. Here, we integrate single-cell RNA sequencing and spatial transcriptomics, analyzing over 177,000 cells and 35,000 spots across 57 tissue samples. This comprehensive approach facilitates the identification of PitNETs tumor populations and characterizes the reconfiguration of the tumor microenvironment (TME) as PitNETs progress and invade. We trace the trajectory of TPIT-lineage PitNETs and identify an aggressive tumor cluster marked by elevated p53-mediated proliferation and a higher Trouillas classification, both associated with tumor progression. Additionally, we document the heterogeneity of immune stromal cells within PitNETs, particularly noting the enrichment of SPP1+ tumor associated macrophages (TAMs) in invasive tumors. These TAMs facilitate tumor invasion through the SPP1-ITGAV/ITGB1 signaling pathway. Our in-depth single-cell and spatial analysis of PitNETs uncovers the molecular dynamics within the TME, suggesting potential targets for therapeutic intervention.

Pituitary neuroendocrine tumors (PitNETs), commonly referred to as pituitary adenomas, are a heterogeneous group of neoplasms originating from the anterior pituitary gland¹. They are classified into three lineages based on specific transcription factors (TFs): PIT1 (lactotrophs, somatotrophs, and thyrotrophs), TPIT (corticotrophs), and SF1 (gonadotrophs)². Clinical symptoms of functioning tumors typically result from excessive hormone secretion³. Additionally, tumor compressing of adjacent structures, such as the optic nerve, may lead to

headaches or vision impairments. Symptoms vary according to excessive hormonal secretion levels and the specific hormones produced by the tumors.

Current standard treatments for PitNETs typically involve surgery as the first-line approach to relieve local mass effects and systemic endocrine-related symptoms⁴. Medical therapies, such as dopamine agonists like cabergoline for prolactinomas and somatostatin receptor ligands for thyroid-stimulating hormone-secreting and growth

A full list of affiliations appears at the end of the paper. ✉e-mail: huxiaomin@pumch.cn; yaoyong@pumch.cn; chunhong_zheng@bjmu.edu.cn; lulin@pumch.cn

hormone-secreting adenomas, are used as first-line treatments in specific cases^{5,6}. However, about 35% of PitNETs are invasive, leading to incomplete excision and frequent recurrences^{7,8}. Aggressive pituitary tumors (APTs), characterized by refractory to standard treatments, rapid growth, and frequent recurrences, presented significant clinical challenges⁹. Early assessment of tumor aggressiveness is crucial for appropriate intervention.

Several studies have demonstrated that the tumor microenvironment plays a critical role in PitNET biology. Tumor-associated macrophages (TAMs), the predominant immune cells in PitNETs, significantly influence tumor size, proliferation, and invasion^{10–12}. Other cell types, including fibroblasts and endothelial cells, also contribute to tumor progression and invasiveness^{13–15}. However, the complex interactions among immune, stromal, and tumor cells remain largely uncharacterized, highlighting the need for further investigation.

Recent studies have highlighted the important role of tumor heterogeneity and microenvironment in PitNET biology with single-cell RNA sequencing (scRNA-seq) technology. Zhang et al. found significant differences in epithelial-to-mesenchymal transition (EMT) signatures between silent and active corticotroph tumors, marked by increased mesenchymal gene expression and reduced hormonal biogenesis¹⁶. Zheng et al. used scRNA-seq to compare pituitary anterior pituitary glands and PitNETs, revealing links between differentiation status and recurrence patterns¹⁷. Lyu et al. studied the tumor microenvironment of PIT1-positive PitNETs, emphasizing interferon-gamma's (IFN- γ) role in remodeling cancer-associated fibroblasts (CAFs)¹⁸. Yan et al. identified the *PBK* gene's role in tumor cell proliferation and migration using scRNA-seq¹⁹. Despite these advances, understanding the complex interactions within the PitNET tumor microenvironment, especially spatially, remains elusive.

In this work, we present the comprehensive integration of a single-cell atlas and spatial architecture of PitNETs to elucidate tumor heterogeneity related to clinical phenotype, cellular organization, and interactions within the tumor microenvironment (TME). This extensive analysis aims to uncover novel cell markers and intricate interactions among tumor, immune, and stromal cells, providing new avenues for targeted therapies.

Results

Single-cell composition and spatial characterization of pituitary tumors

To elucidate the cellular and spatial architecture of pituitary tumors, we conducted a single-cell sequencing study of 172,510 cells and 35,347 spots from 57 pituitary tissue samples. These included 13 adrenocorticotrophic hormone-secreting adenomas (ACTH), 8 prolactin-secreting adenomas (PRL), 3 growth hormone/prolactin cosecreting adenomas (GH/PRL), 7 growth hormone-secreting adenomas (GH), 6 thyroid-stimulating hormone-secreting adenomas (TSH), 1 thyroid-stimulating hormone/growth hormone cosecreting adenoma (TSH/GH), 6 silent gonadotroph adenomas (SGA), 7 silent corticotroph adenomas (SCA), 1 silent TSH-secreting adenoma (STA), 1 null cell adenoma (NCA), 1 follicle-stimulating hormone adenoma (FSH), and 3 normal pituitary tissues, all confirmed pathologically via MRI (Fig. 1a, Supplementary Fig. 1 and Supplementary Data 1). Each tumor subtype was identified by examining hormone secretion-related genes such as *SST*, *POMC*, *PRL*, *GHI*, *TSHB*, and *FSHB* (Fig. 1b). Unsupervised clustering analysis of the scRNA-seq data revealed six dominant cell clusters across all pituitary tumors (Fig. 1c), including myeloid cells, lymphocytes, fibroblasts, endothelial cells, stem cells, and PitNETs tumor cells (Fig. 1d), consistent with previous findings^{17,20}. Although different pituitary tumor types shared common cellular subtypes, suggesting a conserved cellular composition across diverse PitNETs phenotypes, notable differences were observed between samples. For example, stem cells were predominantly derived from a single patient (TSH1), highlighting sample-specific variability (Fig. 1e).

We used integrated analysis of single-cell and spatial transcriptomics to explore the spatial cellular composition and distribution within PitNETs, using a Shared Nearest Neighbor (SNN) modularity optimization-based clustering algorithm²¹. This approach enabled the annotation of spatial spot data into seven niche clusters based on unique gene signatures (Supplementary Fig. 2a, b, Supplementary Data 2), mainly including the ACTH-enriched (Niche 1), SCA/SGA-enriched (Niche 2), PRL-enriched (Niche 3), GH/TSH-enriched (Niche 4), GH/TSH/immune-mixed (Niche 5), and immune-enriched (Niche 6), aligning with their histologic subtypes. Interestingly, despite deriving from different lineages, SCA and SGA samples clustered together, reflecting their nonfunctional tumor characteristics (Supplementary Fig. 2c). Integrating scRNA-seq and spatial transcriptomic data using the Multimodal Intersection Analysis (MIA) approach²² showed high consistency in cell identities (Supplementary Fig. 2d). For example, ACTH-enriched Niche 1 predominantly contained ACTH tumor cells, while immune-enriched Niche 6 was composed of myeloid cells, lymphocytes, fibroblasts, and endothelial cells. Notably, Niche 5, a mixture of GH, TSH, and immune cells, was positioned between the immune and GH/TSH niches, suggesting a transitional state from stromal to cancerous regions.

PitNETs tumor cell transcriptome profile at single-cell resolution

To further investigate PitNET tumor cell characteristics at the single-cell level, we conducted unsupervised cluster analysis by integrating all samples without using batch effect removal algorithms like Harmony²³, which might excessively normalize tumor heterogeneity. In total, 45 distinct clusters were identified in the scRNA-seq data (Fig. 2a). Most clusters displayed an individual-based pattern, except for Cluster 39, which comprised proliferated tumor cells from multiple samples (Supplementary Fig. 3a), highlighting the diversity within PitNETs. Notably, we identified various normal pituitary cell subtypes, including lactotrophs, thyrotrophs, somatotrophs, corticotrophs, gonadotrophs, and undifferentiated PIT1 lineage cells, in normal pituitary tissues (Supplementary Fig. 3b). Differentially expressed genes between tumor cell types and their corresponding normal counterparts revealed upregulation of genes associated with proliferation and invasiveness in tumor cells, such as *TIMP1*, *MYO6*, *CCND1*, and *CCND2*, indicating distinct cellular transcriptomic profiles between tumor and normal cells (Supplementary Fig. 3c). Subsequent scRNA-seq-based copy number variation (CNV) analysis of these clusters revealed chromosomal amplifications and deletions, effectively differentiating cancer cells from nonmalignant cells in normal pituitary tissue. The observed CNV patterns were predominantly individual-specific (Fig. 2b), underscoring the unique genetic landscape of each tumor.

Correlation-based clustering analysis of transcriptional profiles annotated all tumor clusters into six major transcriptional categories: PRL-associated, GH-associated, ACTH-associated, SCA-associated, TSH-associated, and other non-functional adenoma-associated subtypes, according to their marker genes (Fig. 2c, Supplementary Data 3). Tumors from the same lineage showed higher transcriptional similarities and tended to aggregate, with most PIT1 lineage clusters (PRL-, GH-, and GH/PRL-associated) showing strong correlation. Interestingly, TSH-secreting adenomas of the PIT1 lineage exhibited similarities to other nonfunctional PitNETs, such as SGA, indicating a divergent developmental trajectory for TSH tumors compared to other PIT1 lineage tumors. Furthermore, null cell adenoma (NCAs), a nonfunctioning subtype, demonstrated transcriptomic profiles similar to SGAs but also exhibited distinct features, including elevated expression of the differentiation repression gene *HOPX* and tumor progression-related genes *PLCG2* and *TCN2*^{24–26} (Supplementary Fig. 3d). These unique molecular characteristics may contribute to the more invasive behavior observed in NCAs.

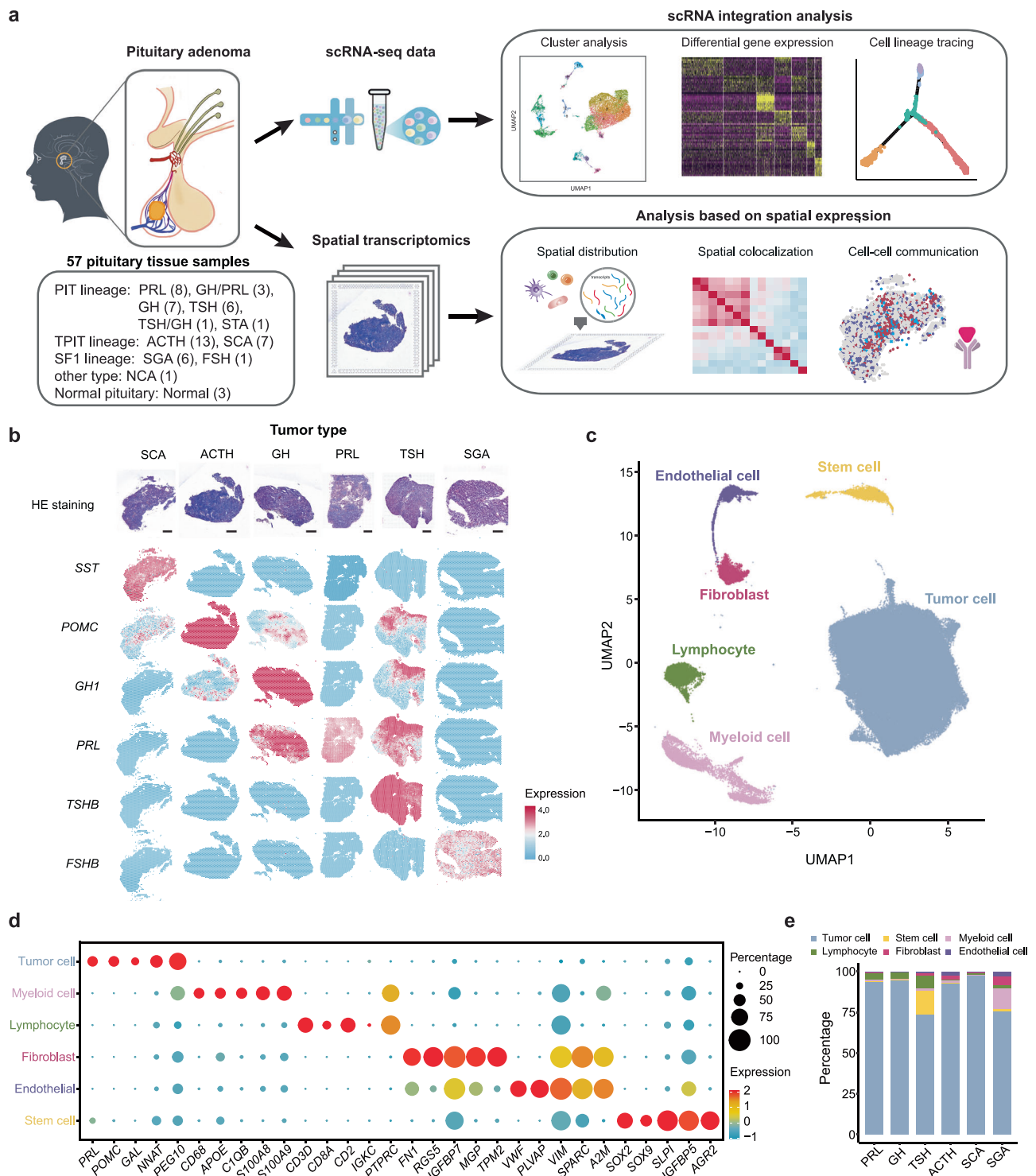


Fig. 1 | Single-cell transcriptome and spatial profiling of PitNETs. a Overview of the study design depicted schematically. Created in BioRender. su, w. (2025) <https://BioRender.com/7d5vph>. **b** H&E staining alongside visualization of single-cell spatial distribution of marker genes in PitNET. Scale bars, 1 mm. **c** UMAP plot illustrating the distinct cell clusters identified by scRNA-seq ($n = 172,510$ cells from

37 samples). **d** Bubble heatmap showing the marker genes for each cell cluster identified through scRNA-seq. **e** Stacked bar plot representing the proportions of major cell populations across different tumor subtypes. Source data are provided as a Source Data file for (d).

Despite high concordance between clinical diagnoses and single-cell transcriptomic profiles for most clusters, some exceptions were noted. For example, two clusters from the SCA1 sample resembled ACTH-associated subtypes at the transcriptomic level, as evidenced by elevated expression of ACTH-specific genes *POMC* and *GAL*, but not

SCA-related genes *GZMK* and *CITED1* (Fig. 2d). Spatial transcriptomic analysis corroborated these unique gene expression patterns in SCA1 (Fig. 2e). Similarly, cells from ACTH6 displayed a complex transitional state between ACTH and SCA tumors, and cells from ACTH5 showed a blend of ACTH- and PRL-associated gene expression (Supplementary

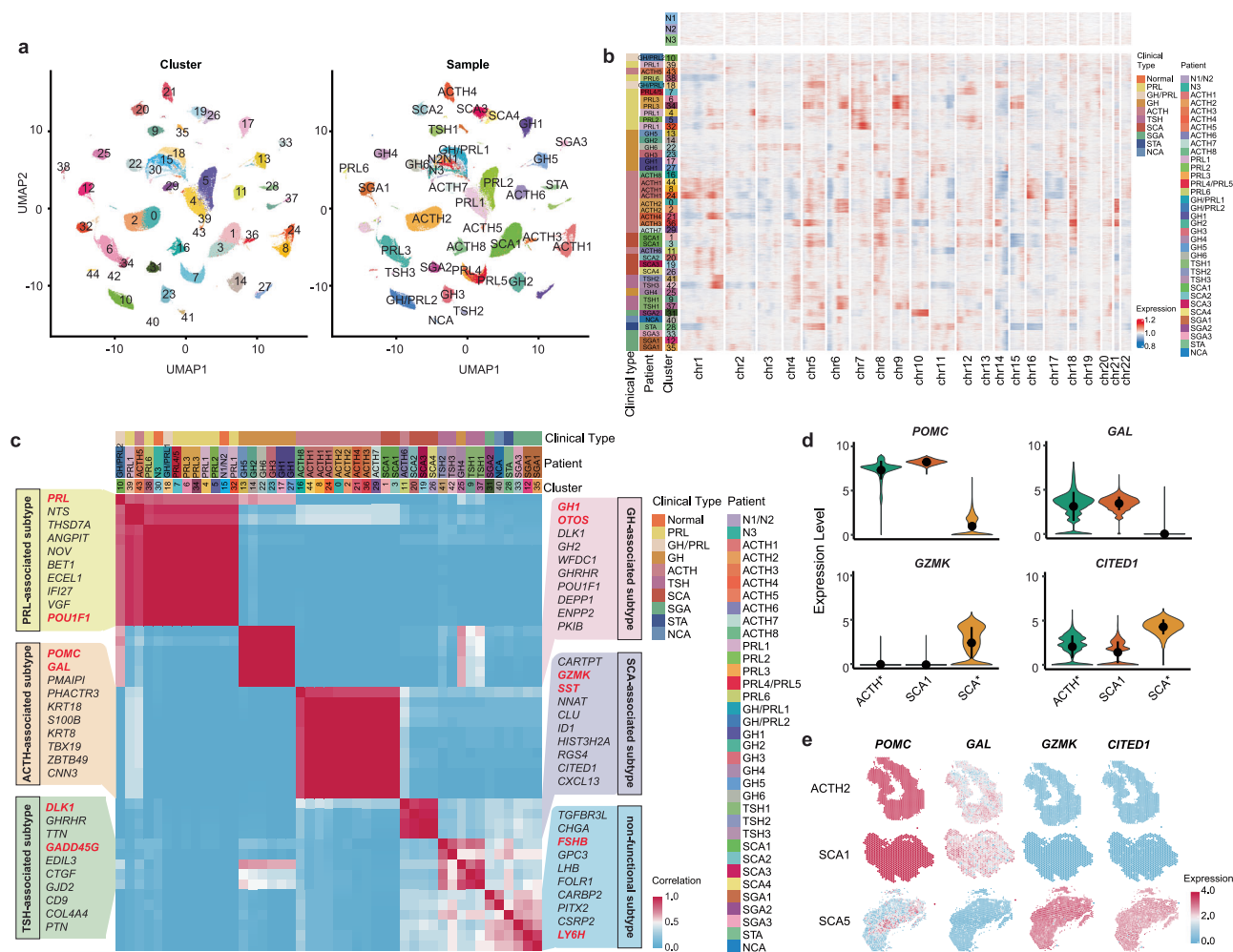


Fig. 2 | Tumor-associated signatures of PitNETs at single-cell resolution.

a UMAP plot showing the distribution of pituitary tumor and normal cell populations ($n = 160,243$ cells from 37 samples). **b** Heatmap of copy number variations (CNVs) in single pituitary cells from normal (top) and tumor (bottom) tissues, inferred from scRNA-seq data. **c** Heatmap depicting Pearson correlation among PitNET tumor clusters ($n = 160,243$ cells), with color intensity representing

correlation strength. **d** Violin plot displaying gene expression profiles for regular ACTH adenomas (ACTH*, including ACTH1, ACTH2, ACTH3, ACTH4, ACTH7, ACTH8), SCA1 and regular SCAs (SCA*, including SCA2, SCA3, SCA4). Data are presented as mean values \pm SD. **e** Spatial gene expression patterns in ACTH2 (a regular ACTH adenoma), SCA1, and SCA5 (a regular SCA tumor). Source data are provided as a Source Data file for (c).

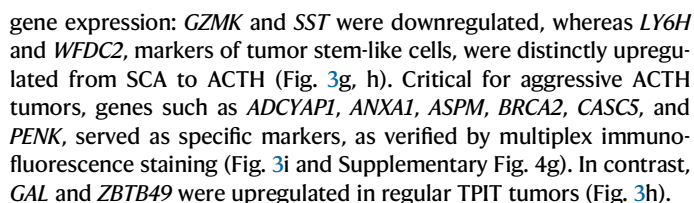
Fig. 3e, f), indicating a multifaceted intrinsic identity beyond standard clinical assessments. These findings underscore the complexity and heterogeneity within PitNETs, and highlight the importance of integrated transcriptomic analyses for accurate tumor characterization.

Identification of aggressive tumor cells in TPIT samples

Given that tumor cells from different PitNETs lineages develop differently, we explored tumoral heterogeneity within each lineage separately. Single cells from 16 TPIT tumor clusters were classified into six groups through hierarchical clustering analysis (Fig. 3a, Supplementary Fig. 4a, and Supplementary Data 4). The TPIT^{pro} and ACTH^{agg} groups demonstrated elevated expression of proliferation markers such as *CENPF*, *TOP2A*, *PTTG1*, *PBK*, and *MKI67*, associated with significantly higher cell cycle, proliferation, and DNA repair activities compared to other clusters (Fig. 3b and Supplementary Fig. 4b). Pathway analysis revealed substantial enrichment in cell cycle and DNA replication pathways within these groups (Fig. 3c, d). However, the ACTH^{agg} group, expressing 82 genes linked to aggressive tumor behavior including *CASC5* and *GTSF1*, showed enhanced p53 and FoxO pathway activity, highlighting their role in tumor progression (Fig. 3c, e). The ACTH^{gro} cluster displayed elevated expression of

PAPPA2 and *AXNA1*, which are crucial for tumor growth and immune evasion^{27,28}. The ACTH^{stem} group, mainly from cluster 16, displayed significant stemness, with high levels of *SOX4* and *LY6H*, indicating a stem-like identity (Supplementary Fig. 4c). Conversely, the ACTH^{reg} and SCA^{reg} groups consisted of Regular TPIT tumor cells, respectively. The ACTH^{reg} tumors were categorized into subgroups based on the expression of genes associated with hormone secretion (e.g., *LGALS3*, *PCSK1*), epithelial-mesenchymal transition (*CDH2*), or developmental pathways (*IGF2*, *GJA1*) (Supplementary Fig. 4d). The SCA^{reg} tumors were classified into subgroups based on varying expression levels of immature TPIT lineage-related genes, including *CARTPT*, *GZMK*, and *SST* (Supplementary Fig. 4e). These findings highlight the internal diversity within regular ACTH and SCA tumors.

We used Monocle 2 to model the developmental trajectories of these groups, revealing a branched structure where SCA^{reg} cells formed the root, emphasizing their silent TPIT tumor identity. ACTH^{stem} cells occupied an intermediate position, suggesting a transition from silent to functioning states. Notably, ACTH^{reg} positioned at one trajectory end, with the remaining three ACTH groups at the opposite, illustrating diverse differentiation paths (Fig. 3f and Supplementary Fig. 4f). Key transitions were underscored by differential



Given the distinct differentiation pathway observed in ACTH tumors, we investigated the principal drivers of their development. Two atypical ACTH tumor subgroups, ACTH^{Agg} and ACTH^{Gro}, comprised exclusively of cells from a single patient, ACTH1, who experienced exceptionally aggressive tumor progression (Fig. 4a). Following surgical intervention, serum cortisol and ATCH levels initially decreased

Fig. 3 | Characterization of tumor cells in TPIT samples. **a** Heatmap displaying specific gene expression profiles across six TPIT tumor subtypes. **b** Boxplots illustrating cell cycle (left), proliferation (middle), and DNA repair (right) scores for each TPIT tumor subtype. Boxes span the interquartile range (IQR) and whiskers extend to points that lie within 1.5 IQRs of the lower and upper quartile. Center line is drawn at the median. Statistical analysis was performed using the two-sided Kruskal–Wallis test. For **(a)** and **(b)** a total of 70,196 cells from 12 samples were analyzed across six groups: TPIT^{Pro} ($n = 378$), ACTH^{Agg} ($n = 217$), ACTH^{Gro} ($n = 7,725$), ACTH^{Stem} ($n = 3,789$), ACTH^{Reg} ($n = 44,079$), and SCA^{Reg} ($n = 14,008$). **c** Venn diagram showing the overlap of marker genes between TPIT^{Pro} and ACTH^{Agg} groups. **d** KEGG pathway enrichment analysis of common genes shared by TPIT^{Pro} and ACTH^{Agg}

groups. One-sided Fisher's exact test. **e** KEGG pathway enrichment analysis of genes specific to ACTH^{Agg} group. One-sided Fisher's exact test. **f** Developmental trajectory of TPIT tumor cells as inferred by Monocle2, with each dot representing a cell. **g** Branched heatmap showing significant gene expression changes over pseudo-time, with genes indicated on top. **h** Gene expression trends for selected genes along the trajectory. **i** Representative multiplex immunofluorescence staining of ACTH1 (aggressive ACTH tumor) and ACTH2 (non-aggressive ACTH tumor), each with 3 technical replicates. Individual and merged channels are shown for DAPI, ANXA1, CASC5, ASPM, BRCA2, ADCYAP1, and PENK. Scale bar, 100 μm . Source data are provided as a Source Data file for **(b)** and **(c)**.

transiently (Fig. 4b). However, the patient's progression-free survival was markedly brief, lasting only 15 months, significantly shorter compared to other ACTH tumor cases (Fig. 4c). Subsequent attempts to manage tumor progression through additional surgeries proved largely ineffective, with only temporary reductions in serum cortisol and ACTH levels followed by a sharp increase. Unfortunately, the patient succumbed rapidly to complications from Cushing's disease. Retrospective immunohistochemistry (IHC) analysis revealed that the patient was p53 positive, with an exceptionally high Ki67 positivity rate of 8% (Fig. 4d, e). Notably, according to the Trouillas classification, the four regular ACTH-secreting tumors were classified as grade 1a, while tumor ACTH1 was classified as grade 2b (Fig. 4d), indicating a more aggressive behavior in tumor progression.

Interestingly, cells in the ACTH^{Agg} subgroup from patient ACTH1 exhibited similar gene expression patterns with *TP53* and *MKI67*. These cells specifically overexpressed cell cycle-related genes in the *p53* signaling pathway (Fig. 4f, g), including *CCNB1*, *CDK1*, *CCNB2*, *CCND3*, and *CDK2*, and showed significantly higher *p53*-cell cycle scores compared to other clusters (Fig. 4h). This suggested that cell cycle signaling within the *p53* pathway may contribute to the aggressive nature of ACTH tumors. An independent cohort study, including data from all pituitary ACTH tumor patients who underwent surgery at Peking Union Medical College Hospital (PUMCH) between January 2018 and January 2022, revealed that patients with both p53 positivity and a high Ki67 index experienced markedly shorter postoperative recurrence internals (Fig. 4i), indicating a faster growth rate and increased tumor aggressiveness. Additionally, whole-exome sequencing of tumor samples from patients ACTH1 and ACTH2 revealed that they both harbored the TP53 Pro72Arg mutation, a common mutation in ACTH tumors²⁹. Notably, the TP53 Arg248Gln hotspot mutation was detected exclusively in patient ACTH1 (Fig. 4j), a mutation known to enhance motility and invasive potential compared to other mutations³⁰, potentially driving the proliferation of aggressive ACTH tumor cells.

Tumor heterogeneity of PIT1 and SF1 lineage

We further investigated the heterogeneity of tumor cells within the PIT1 and SF1 lineages, identifying six distinct tumor subgroups within PIT1 and two within SF1, each with unique molecular signatures (Supplementary Fig. 5a, b). The PRL^{Pro} subgroup exhibited elevated levels of cell proliferation markers, including *PTTG1*, *CENPF*, and *TOP2A*, and significantly higher cell cycle and proliferation scores compared to other subgroups (Supplementary Fig. 5c). Notably, the PIT1^{Pro} subgroup specifically expressed *GGH* and *PBK*, which Yan et al. identified as inhibitors of pituitary tumor cell apoptosis and promoters of cell proliferation¹⁹. These cells predominantly originated from cluster 39 of patient PRL1, who was resistant to bromocriptine, aligning with studies showing that high *PBK* expression correlates with a worse prognosis³¹. The PRL^{Growth} subgroup displayed specific expression of tumor growth-associated genes, including *IGF1* and *SHC1*^{32,33}. Conversely, the PRL^{Adhesion} subgroup was characterized by the expression of genes related to adherens junctions, such as *RAP1B*

and *MYL12A*³⁴. The TSH^{Undiff} subgroup, primarily from STA, showed high expression of *IGFBP7* and *GATA2* (Supplementary Fig. 5d), indicative of a transcriptional profile resembling immature PIT1 pituitary lineage tumors, and also exhibited a higher stemness score. Cells in the PRL^{Reg} and TSH/GH^{Reg} groups corresponded to regular PRL and TSH/GH tumors, respectively, and were further classified based on tumor hormone expression, particularly *GHI* and *PRL* (Supplementary Fig. 5e, f). This classification highlighted the internal heterogeneity within regular PIT1 tumors.

In the SF1 lineage, SF1^{Reg} cells exhibited high expression of gonadotroph hormone-related genes *LHB*. However, these cells displayed varying levels of *FSHB* expression, which has been associated with different cell types during the development of normal pituitary gonadotrophs³⁵ (Supplementary Fig. 5g). This variation suggests the heterogeneity present within the regular SF1 lineage tumor cells. The SF1^{Undiff} subgroup was characterized by high expression of genes associated with poorly differentiated SF1 lineage tumors, such as *GPC3* and *SIX2*. Interestingly, we observed that SF1^{Undiff} cells shared several co-expressed genes with other stem-like or undifferentiated subtypes TSH^{Undiff} and ACTH^{Stem} (Supplementary Fig. 5h). Specifically, *WFDC2*, a gene highly expressed in early human embryonic stem cell-derived trophoblasts³⁶ as well as pituitary stem cells in this study, was consistently upregulated (Supplementary Fig. 5i). Furthermore, *NFIX*, *IGFBP5*, and *TESC*, known regulators of stem cell behavior, were also commonly expressed^{37–39}. These findings point to a shared stem-like signature among these subtypes, irrespective of lineage.

The diverse tumor immune microenvironment in PitNETs

We performed a comprehensive single-cell analysis of the tumor immune microenvironment in PitNETs. Immune stromal cells were classified into 16 distinct clusters, including NK cells, T cells, B cells, tumor-associated macrophages (TAMs), cancer-associated fibroblasts (CAFs), neutrophil, monocytes, type-2 conventional dendritic cells (cDC2), and endothelial cells (ECs) (Fig. 5a and Supplementary Fig. 6a). Notably, two EC subtypes were identified: arterial ECs, characterized by *IGFBP3*, *GJAS* and *LTBP4*, and venous ECs, marked by *PLVAP*, *NRP2*, and *VWAI*^{40–42} (Fig. 5b and Supplementary Fig. 6b). We also identified three CAF subpopulations: cancer-associated myofibroblasts (CAF_{Myo}), expressing *NDUFA4L2* and *MYH11*; inflammatory CAFs (CAF_{Infla}), characterized by collagen-encoding genes *COL1A1* and *COL1A2*; and endothelial-to-mesenchymal transition CAFs (CAF_{Emt}), exhibiting markers of both CAFs and ECs, such as *RGSS5* and *PLVAP*, indicative of a transitional phenotype⁴³ (Supplementary Fig. 6c).

TAMs were further categorized into three distinct subtypes based on their gene expression profiles. The TAM_{IER2} cluster demonstrated a pro-inflammatory phenotype with expression of *EGR1*, *FOS*, and *JUN*⁴⁴. The TAM_{SEPP1} cluster resembled tissue-resident macrophages, characterized with *SEPP1* and *SLC40A1* expression⁴⁵. A unique gene expression profile was observed in SPPI+ TAMs (Fig. 5c). Gene enrichment analysis revealed significant upregulation of PPAR and TNF signaling pathways (Fig. 5d), with increased expression of *OLR1*, *PLIN2*, *FABP5*, *NFKB1*, and pro-inflammatory cytokines *CCL2* and *CCL20*^{46,47}

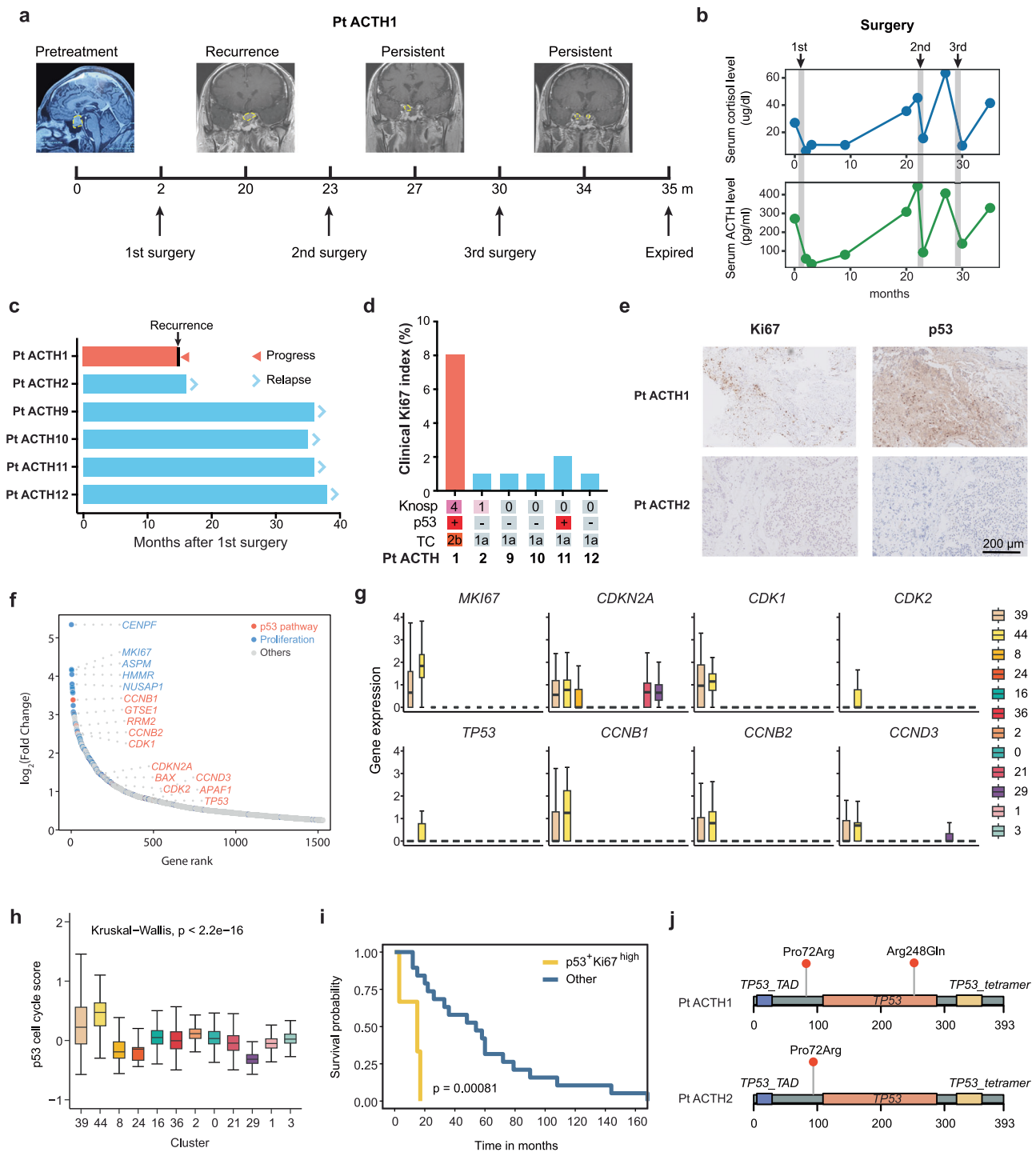
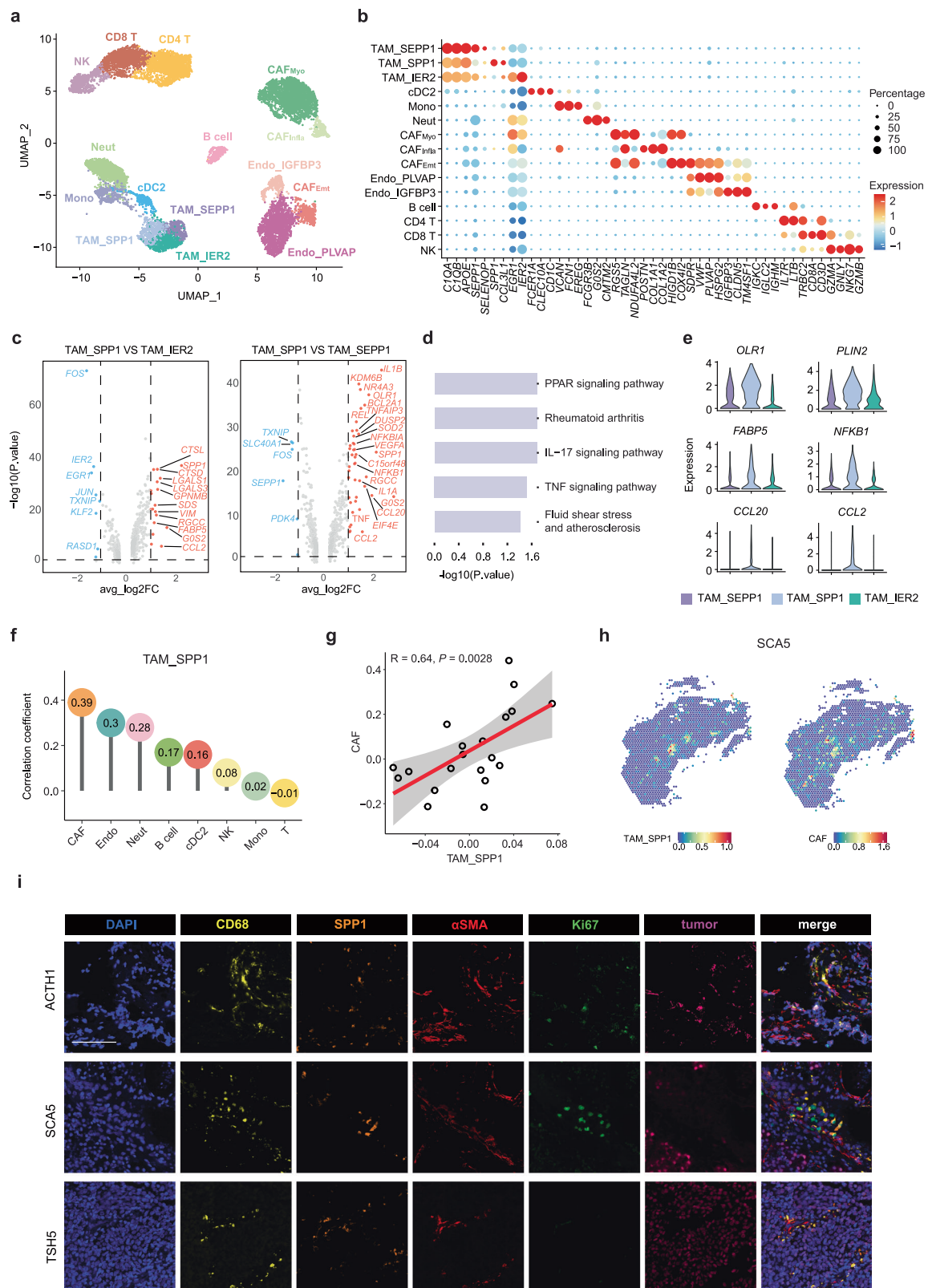


Fig. 4 | Clinical and molecular features of aggressive ACTH tumors. a Timeline of diagnosis, treatment, recurrence, and persistence for patient ACTH1, with MRI images at key points and tumor borders outlined in yellow dashed lines. **b** Serum cortisol and ACTH levels during the treatment of patient ACTH1. **c** Bar plot of recurrence time after initial surgery for ACTH patients. **d** Bar plot of Ki67 index, Knosp grade, p53 IHC staining, and Trouillas classification (TC) in ACTH patients. **e** IHC staining of Ki67 and p53 in tissue sections from patients ACTH1 and ACTH2 ($n = 3$ technical replicates for each patient). **f** Gene-rank plot of marker genes in cluster 44, with p53 pathway genes in red and proliferation-related genes in blue. **g** Expression of cell cycle-related p53 pathway genes across clusters. Boxes span the interquartile range (IQR) and whiskers extend to points that lie within 1.5 IQRs of

the lower and upper quartile. Center line is drawn at the median. **h** Boxplot of p53-associated cell cycle scores by cluster, using the Kruskal–Wallis test. Boxes span the interquartile range (IQR) and whiskers extend to points that lie within 1.5 IQRs of the lower and upper quartile. Center line is drawn at the median. For (**g**, **h**) a total of 54,607 cells were analyzed across 12 clusters: 0 ($n = 11,109$), 1 ($n = 9,127$), 3 ($n = 8,674$), 8 ($n = 5,033$), 11 ($n = 4,455$), 16 ($n = 3,789$), 21 ($n = 3,021$), 24 ($n = 2,692$), 29 ($n = 2,291$), 36 ($n = 851$), 39 ($n = 378$), and 44 ($n = 217$). **i** Kaplan–Meier progression-free survival curves for 18 patients with tumor recurrence, stratified by p53 staining and Ki67 index, analyzed by log-rank test. **j** Lollipop plot showing TP53 mutation sites in patients ACTH1 and ACTH2. Source data are provided as a Source Data file for (**h**) and (**i**).



(Fig. 5e), suggesting a crucial role for SPP1+ TAMs in PitNETs. Interestingly, the composition and proportions of immune and stromal cell subpopulations showed no significant differences between tumor and normal tissues (Supplementary Fig. 6d).

To elucidate the spatial organization of immune stromal niches, we employed spatial transcriptomics to delineate the distribution of

each cell type. Analysis of spatial correlation coefficients across all ST samples indicated that SPP1+ TAMs showed the most pronounced spatial association with CAFs compared to other cell types (Fig. 5f). This pattern was also consistently observed in individual samples (Fig. 5g, h), highlighting a significant spatial interaction between SPP1+ TAMs and CAFs. Subsequent immunofluorescent labeling

Fig. 5 | Single-cell tumor immune microenvironment in PitNETs. **a** UMAP plot showing the distribution of tumor immune microenvironment in PitNETs, colored by their cell types ($n = 12,267$ cells from 37 samples). **b** Bubble heatmap showing marker genes across 15 cell clusters through scRNA-seq ($n = 12,267$ cells from 37 samples). **c** Volcano plot showing differentially expressed genes between TAM_SPP1 versus TAM_IER2 (left), and TAM_SPP1 versus TAM_SEPP1 (right). A total of 1,367 TAMs were analyzed, including TAM_SEPP1 ($n = 269$ cells), TAM_SPP1 ($n = 456$ cells), and TAM_IER2 ($n = 642$ cells). Two-sided unpaired limma moderated t -test. **d** The pathway enrichment analysis of upregulated genes by TAM_SPP1. One-sided Fisher's exact test. **e** Violin plot showing upregulated genes of TAM_SPP1 in TAM clusters. **f** Lollipop plot showing the spatial correlation coefficient between TAM_SPP1 cluster score and other dominant immune cell cluster scores

($n = 35,347$ spots from 20 samples). Spearman-correlation test. **g** Scatter plot showing the correlation between the infiltration of TAM_SPP1 and CAFs based on the average GSVA scores for each spatial transcriptomic (ST) sample ($n = 20$). Each circle represents one ST sample. The error band indicates a 95% confidence interval, the mean was used as the center for the error bars. Two-sided spearman-correlation test. **h** Spatial feature plots of signature score of TAM_SPP1 and CAFs in tissue sections. **i** Representative multiplex immunofluorescence staining of human PitNET tumors. DAPI (blue), CD68 (yellow), SPP1 (orange), α SMA (red), Ki67 (green), and tumor markers ACTH (ACTH1), TPIT (SCA5), and PIT-1 (TSH5) (magenta) are shown in individual and merged channels. Experiment was performed in three independent patients, each with three technical replicates. Scale bar, 100 μ m. Source data are provided as a Source Data file for (c) and (e).

further confirmed the close proximity of SPP1+TAMs and CAFs in PitNETs tissues (Fig. 5i). Moreover, genes highly expressed in SPP1+ TAM/CAF colocalization spots were significantly enriched in pathways involving cell adhesion molecules, focal adhesion, and complement coagulation cascades (Supplementary Fig. 6e), such as *FN1*, *SERPING1* and *MYL9*, which were also validated by multiplex immunofluorescence staining (Supplementary Fig. 6f, g). This enrichment pattern suggests a close interaction and potential collaboration between SPP1+ macrophages and CAFs in ECM remodeling in PitNETs.

The association between SPP1 + TAMs and PitNET invasion

To assess the clinical significance of immune stromal cell clusters, we determined their enrichment across samples using the ratio of observed to expected (Ro/e) analytical method^{48,49} (Fig. 6a). Notably, SPP1+ TAMs were significantly enriched in invasive pituitary tumors, independent of tumor size, relapse status, and PitNET subtypes (Fig. 6b–d and Supplementary Fig. 6h). This finding was corroborated using two published bulk sequencing datasets^{50,51}, where the prevalence of invasive pituitary tumors was markedly higher in the SPP1^{high} group compared to the SPP1^{low} group (Fig. 6e). Furthermore, we assessed the correlation between invasiveness and SPP1+ TAM in an independent cohort of 47 patients using multiplex immunofluorescence staining data (Fig. 6f). The result revealed that the percentage of SPP1+TAMs was significantly higher in invasive patients compared to non-invasive patients, consistent with our single-cell RNA-seq findings.

To further explore the potential role of SPP1+ TAMs in tumor invasion, we quantified the molecular interactions between SPP1+ TAMs and tumor cells from both invasive and noninvasive PitNETs. Among the top five enriched ligand-receptor pairs, the SPP1-ITGAV/ITGB1 interaction was most pronounced between SPP1+ TAMs and invasive tumors, rather than non-invasive ones (Fig. 6g, h). Additionally, invasive tumors exhibited elevated MAPK and PI3K/Akt pathway scores, key downstream effectors of integrin signaling (Fig. 6i). Spatial transcriptomic analysis showed a higher prevalence of co-localized spots expressing SPP1, ITGAV and ITGB1 in invasive samples compared to non-invasive ones (Fig. 6j), a result corroborated by multiplex immunofluorescence staining (Fig. 6k). This suggests that SPP1+ TAMs may facilitate tumor invasion by engaging with tumor cells through the SPP1-ITGAV/ITGB1 pathway, thereby enhancing cell adhesion and migration.

To investigate the role of secreted SPP1 (osteopontin) in promoting invasive PitNET tumors, we conducted in vitro analyses using three common PitNET cell lines: GH3, AtT20, and TtT/GF. Cell proliferation, wound healing, and trans-well invasion assays were employed to assess the effects of SPP1. The CCK-8 assay confirmed that osteopontin significantly promoted cell proliferation in all PitNET cell lines (Fig. 7a). Additionally, wound healing and trans-well invasion assays demonstrated that osteopontin (OPN) enhanced cell migration and invasion (Fig. 7b–e).

To further validate these findings, we established primary pituitary tumor and PitNET organoid models derived from two independent patients, both of which retained key tumor characteristics (Fig. 7f). SPP1 treatment not only promoted pituitary tumor migration and invasion (Fig. 7g–h), but also significantly enhanced cell growth and increased Ki67 expression in PitNET organoids (Fig. 7i–k). Notably, SPP1-treated organoids exhibited increased collective invasion into collagen gels, as evidenced by a greater number of multicellular protrusions (Fig. 7i).

To explore the role of ITGB1 in mediating the tumor-promoting effects of SPP1, we knocked down ITGB1 expression in GH3, AtT20, and TtT/GF cell lines (Fig. 8a–b). CCK-8 and trans-well invasion assays revealed that ITGB1 knockdown significantly reversed SPP1-induced cell proliferation and invasion across all three cell lines (Fig. 8c–e). These results demonstrated that SPP1 exerted its tumor-promoting effects on PitNET cells through its interaction with ITGB1.

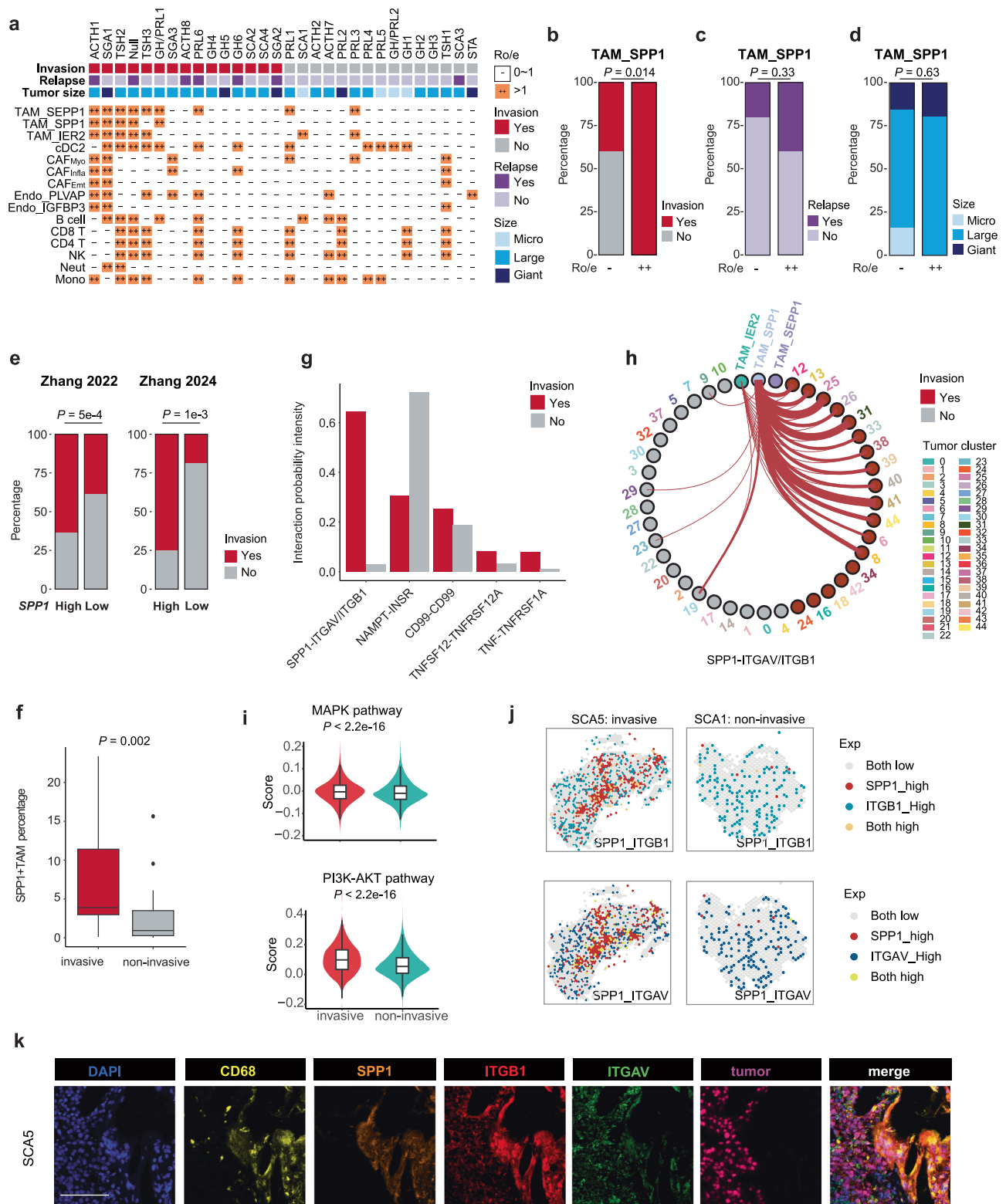
Collectively, our scRNA-seq data and in vitro assays indicate that TAMs may exert important functions by interacting with different immune and stromal cells within the PitNET TME.

Discussion

In our study, we employed a multi-omics approach to investigate the complexities of pituitary tumor heterogeneity, encompassing single-cell RNA and spatial transcriptomics sequencing. This study presents an integrated scRNA-seq and ST investigation of pituitary tumors, offering detailed insights into their biological landscape.

PitNETs are prevalent intracranial neoplasms with a range of clinical presentations. While standard treatments such as surgery, radiotherapy, and pharmacotherapy are available, managing aggressive PitNETs (APTs) remains challenging due to their tendency for rapid relapses. Notably, the ACTH-secreting PitNETs subtype, more prevalent among APTs, is linked to severe hypercortisolemia and a poor prognosis⁹. Early detection and intervention are crucial for improving outcomes and preventing tumor recurrence. However, the current diagnosis paradigm, which relies on evolving clinical phenotypes, lacks predictive biomarkers for the transition from non-aggressive to aggressive PitNETs. Temozolomide, the recommended chemotherapy for APTs, has limited efficacy, highlighting an urgent need for a deeper understanding of APT pathogenesis and the identification of novel therapeutic targets⁵².

While p53, Ki67 and Trouillas classification have traditionally been used as markers for assessing tumors with malignant potential, the clinicopathological correlations between these markers and tumor aggressiveness remain limited. This highlights the need for advanced molecular approaches to better predict and elucidate aggressive tumor behavior. Our scRNA-seq analysis extends beyond conventional markers by identifying a novel ACTH^{Agg} cluster that may serve as a biomarker for early detection of APTs. This cluster, distinct in its proliferative activity and association with the p53 signaling pathway, sets it apart from general proliferative groups. Notably, the identification of genes like *CCNB1* and *CCNB2*, along with known APT markers



(*PTTG1*, *CCND1*, *TOP2A*), provides molecular indicators for assessing PitNET aggressiveness.

It is well-established that mutations in specific genes play a crucial role in the tumorigenesis and progression of pituitary tumors. For example, USP8-mutant tumors are characterized by smaller tumor size and increased ACTH production compared to wild-type PitNETs⁵³. Mutations in *GNAS* are associated with elevated preoperative IGF-1 levels, lower invasiveness, and improved surgical remission rates^{51,54}. AIP mutations are linked to Familial Isolated Pituitary Adenomas

(FIPA), with tumors in these patients exhibiting more aggressive behavior than those in AIP-negative individuals⁵⁵. Notably, the ACTH^{Agg} cluster in this study predominantly arises from a patient with a TP53 R248Q mutation, a known hotspot that confers a gain-of-function effect and is implicated in tumorigenesis, invasion, and metastasis across various cancers^{30,56,57}. This mutation has been specifically associated with an ACTH-secreting pituitary carcinoma with metastases to the liver and thoracic vertebrae⁵⁸. Targeting the p53 pathway in APT therapy could be a promising strategy, including the use of

Fig. 6 | SPP1 + TAM and tumor invasiveness in PitNETs. **a** Prevalence of each immune stroma cluster, estimated by Ro/e score. **b–d** Proportions of patients with different invasion (**b**), relapse (**c**) and size (**d**) statuses comparing TAM_SPP1-enriched ($n = 5$) versus TAM_SPP1-depleted ($n = 25$) groups. P -values were determined by two-sided chi-square test. **e** Patient proportions with varying invasion statuses, using bulk sequencing data from Zhang 2022⁵¹ ($n = 80$ (SPP1 high) and 114 (SPP1 low)) and Zhang 2024⁵⁰ ($n = 16$ (SPP1 high) and 16 (SPP1 low)). p -values calculated by two-sided chi-square test. **f** Bar plot showing the proportion of SPP1+ TAMs in invasive ($n = 14$) and non-invasive ($n = 33$) PitNETs, as determined by multiplex immunofluorescence staining data. p -value was calculated using the two-sided wilcoxon signed-rank test. Boxes span the interquartile range (IQR) and whiskers extend to points that lie within 1.5 IQRs of the lower and upper quartile. Center line is drawn at the median. **g** Bar plot of top 5 ligand-receptor pairs with the highest interaction probabilities between invasive and noninvasive PitNETs.

h Chord diagrams illustrating interactions between TAM subtypes and tumor clusters via SPP1-ITGAV/ITGB1 ligand-receptor pair, with line width indicating interaction intensity. **i** Signature scores of MAPK pathways (top) and PI3K-AKT pathways (bottom) for invasive ($n = 44,607$ cells) and non-invasive ($n = 103,032$ cells) tumor clusters. p -values were determined using the two-sided wilcoxon signed-rank test. Boxes span the interquartile range (IQR) and whiskers extend to points that lie within 1.5 IQRs of the lower and upper quartile. Center line is drawn at the median. **j** Spatial gene expression patterns of *SPP1*, *ITGAV*, and *ITGB1* in samples SCA5 (invasive tumor) and SCA1 (non-invasive tumor). **k** Representative multiplex immunofluorescence staining of human PitNET tissue. DAPI (blue), CD68 (yellow), SPP1 (orange), ITGB1 (red), ITGAV (green), and tumor marker TPIT (magenta) are shown in individual and merged channels ($n = 3$ biological replicates). Scale bar, 100 μm . Source data are provided as a Source Data file for (a–i).

compounds that restore p53 function and gene therapy approaches with viral vectors, nanoparticles, and p53 mutant-specific siRNAs⁵⁹.

The tumor microenvironment significantly influences tumor behavior and patient outcomes⁶⁰. Our integrative analysis, combining scRNA-seq and spatial transcriptomics, has delineated a detailed immune stromal cell atlas and the spatial organization of immune stroma niches within PitNETs. A distinct subpopulation of TAMs, the SPP1+ TAMs, with a unique gene expression profile, was found to colocalize with CAFs within the TME. Studies have implicated SPP1+ TAM in promoting a pro-tumorigenic phenotype in various cancer types, including colon cancer, head and neck squamous cell carcinomas, and glioma^{51,61,62}. Our research extends these findings to PitNETs, showing that SPP1+ TAMs enrich TNF pathways and secrete immunosuppressive cytokines CCL2 and CCL20, thus facilitating a pro-inflammatory tumor microenvironment conducive to tumor immune evasion. Moreover, SPP1+ TAM are preferentially enriched in invasive PitNETs and interact with invasive tumor cells through SPP1-ITGAV/ITGB1 ligand-receptor interactions, indicating a role in promoting tumor aggression. Similar interactions between SPP1+ TAMs and cancer stem cells in hepatocellular carcinoma suggest that SPP1+ TAMs may be central to the aggressive behavior of PitNETs, presenting a potential target for therapeutic intervention⁶³. Additionally, in invasive tumors, SPP1+ TAMs and CAFs also showed stronger SPP1-ITGAV/ITGB1 ligand-receptor interactions compared to non-invasive tumors (Supplementary Fig. 6i). Furthermore, ligand-receptor analysis between CAFs and tumor cells demonstrated ECM proteins secreted by CAFs, such as collagen and fibronectin 1 (FN1), exhibit extensive interactions with integrin receptors on invasive tumor cells (Supplementary Fig. 6j). These interactions have been previously shown to promote cell invasion and proliferation^{64,65}, suggesting that CAF-tumor cell communication may also play a critical role in enhancing the metastatic potential of pituitary neuroendocrine tumors.

In summary, our integrative scRNA-seq and spatial transcriptomic analysis has elucidated the heterogeneity of PitNETs and identified distinct cell subtypes and associated molecular markers. These findings contribute to a more refined understanding of PitNET biology and pave the way for the development of targeted treatment strategies.

Methods

Human specimen collection

This study was approved by the Institutional Review Boards of Peking Union Medical College Hospital (Ethical number: I-22PJ933). Written informed consent was obtained from all patients for publication of clinical information. A total of 23 patients consented to sample collection and data analysis. In line with institutional and ethical guidelines, the maximal tumor size or burden permissible for inclusion in the study was determined by the Institutional Review Board. All human tumor samples used in this research were collected within these approved limits. Each sample underwent histological evaluation by an experienced pathologist. PitNETs were classified according to the

World Health Organization (WHO) 2022 criteria, based on immunohistochemistry (IHC) results for three lineage-specific transcription factors (PIT1, SF1, and TPIT) and hormonal expression. Tumor invasiveness was assessed using the Knosp grading system, Hardy-Wilson classification, and Trouillas classification on preoperative magnetic resonance imaging (MRI). Knosp grades 3 and 4, Hardy-Wilson grades 3 and 4 or stage D and E, Trouillas classification grade 2a, 2b and 3 were categorized as invasive tumors. Tumor aggressiveness was defined as the rapid growth of tumors resistant to first-line treatments, necessitating repeated surgeries.

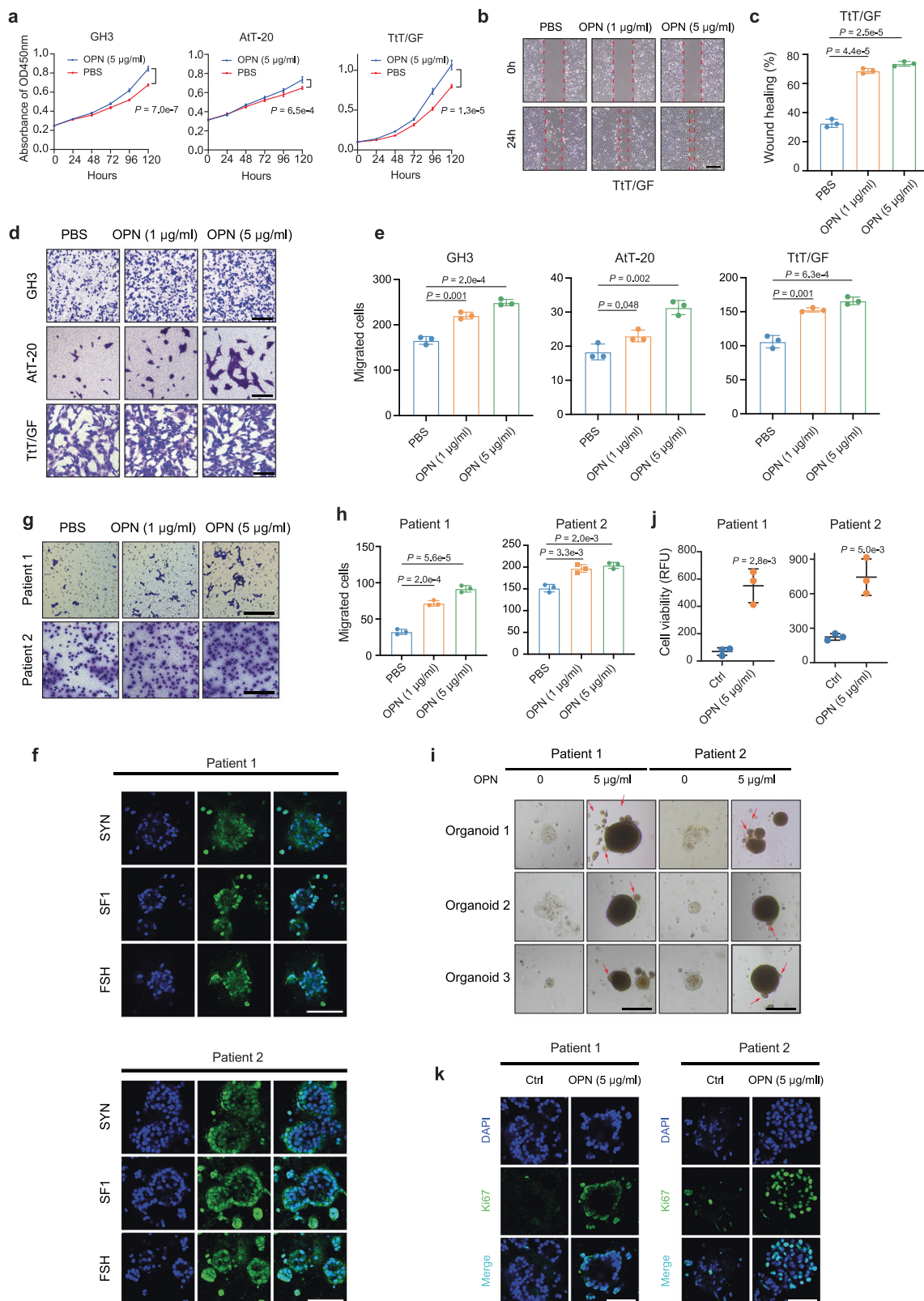
Single-cell RNA sequencing and data processing

Fresh tissue specimens collected post-surgery were preserved in tissue preservation solution (Miltenyi) and promptly processed for single-cell RNA sequencing using 10x Chromium Single Cell 3' reagent kit, following the manufacturer's protocol (10X Genomics). Multiplexed library pools were sequenced on the Illumina NovaSeq6000, generating 150-bp paired-end reads.

Raw FASTQ files were processed with CellRanger software (10X Genomics, v4.0.0) using default settings. Cells were filtered using the Seurat package (v4.1.0) based on the following criteria: a maximum of 15,000 unique molecular identifiers (UMIs), detection of >300 and fewer than 7500 genes, and <30% mitochondrial RNA content. Doublets were identified using DoubletFinder (v2.0.4) with default parameters, and doublet clusters were removed using a cluster-level approach. Specifically, cells in immune and stromal clusters expressing pituitary tumor lineage-specific markers such as *POMC*, *GAL*, *GHI*, and *PRL* were excluded from further analysis.

Then, we merged expression matrices from individual patient samples, followed by log-transformation and scaling to normalize the data. Top 2000 highly variable genes were detected with the FindVariableFeatures function in the Seurat package. Principal component analysis (PCA) was executed, and the initial 15 principal components were selected for further investigation. To address batch effects across patient samples, Harmony (v1.0) was applied to the first round of unsupervised clustering. UMAP coordinates were generated from the neighborhood graphs, and initial cell clustering was achieved using Leiden clustering at a resolution of 0.3. Differential gene expression (DEG) analysis was performed on each cluster using the Wilcoxon algorithm through the FindAllMarkers function, with a one-tailed Wilcoxon rank-sum test and Bonferroni correction for p -value adjustment. Genes exhibiting a fold change >1 and an adjusted p -value below 0.05 were designated as DEGs, which were subsequently used to characterize cell identities.

In the second round of unsupervised clustering, focus shifted to tumor cells identified from the first round. Dimension reduction and graph-based clustering strategies were reapplied, this time for tumor clusters, without the application of batch correction via Harmony. To minimize noise and dissociation-induced expression artifacts, we excluded genes related to mitochondria, heat-shock protein,



ribosomes, and dissociation, as previously described by Xue R et al.⁶⁶. Malignant cell clusters were delineated using SNN-based clustering, leveraging the first 20 principal components at a resolution of 0.8.

CNV estimation of malignant cells with scRNA seq data

Copy number variation (CNV) analysis for individual cells was performed utilizing inferCNV (v.1.16.0) (<https://github.com/broadinstitute/>

inferCNV), employing a 100-gene sliding window approach. Smoothing of the data was achieved using the pyramidal method, and the analysis was conducted on a per-sample basis. During the inferCNV processing, genes exhibiting an average read count of <0.1 in the reference cells were excluded. Normal pituitary tissue-derived cells served as the reference population. To enhance analytical efficiency, down-sampling was applied to both the reference and the observed cell datasets.

Fig. 7 | SPPI (Osteopontin, OPN) promotes proliferation and invasion of pituitary tumor cells. **a** CCK-8 cell viability assay of GH3, AtT-20, and TtT/GF cells treated with OPN or PBS ($n = 5$ biological replicates). Data are presented as mean values \pm SD. **b** Representative images of the wound healing assay, and **(c)** quantitative analysis of TtT/GF cells treated with OPN or PBS ($n = 3$ biological replicates). Data are presented as mean values \pm SD. **d** Transwell invasion assay and **(e)** quantitative analysis of GH3, AtT-20, and TtT/GF cells treated with OPN or PBS ($n = 3$ biological replicates). Data are presented as mean values \pm SD. **f** Immunofluorescence images of PitNET markers (SYN, SF1, FSH) in PitNET organoids from two independent patients ($n = 3$ biological replicates). **g** Transwell invasion assay and **(h)** quantitative analysis of primary pituitary tumor cells

cultured from two independent patients, treated with OPN or PBS ($n = 3$ biological replicates). Data are presented as mean values \pm SD. **i** Bright-field images illustrating representative phenotypes of three independently derived PitNET organoids from each of the two patients treated with OPN or PBS. Arrows indicate cell protrusions in PitNET organoids. **j** CellTiter-Glo luminescent cell viability assay of PitNET organoids treated with OPN or PBS ($n = 3$ biological replicates). Data are presented as mean values \pm SD. **k** Immunofluorescence images of Ki67 in PitNET organoids from two patients treated with OPN or PBS ($n = 3$ biological replicates). For all panels, scale bar, 100 μ m. Two-sided unpaired t -test was performed for **(a–j)**. Data are presented as mean values \pm SD for **(a–j)**. Source data are provided as a Source Data file for **(a–j)**.

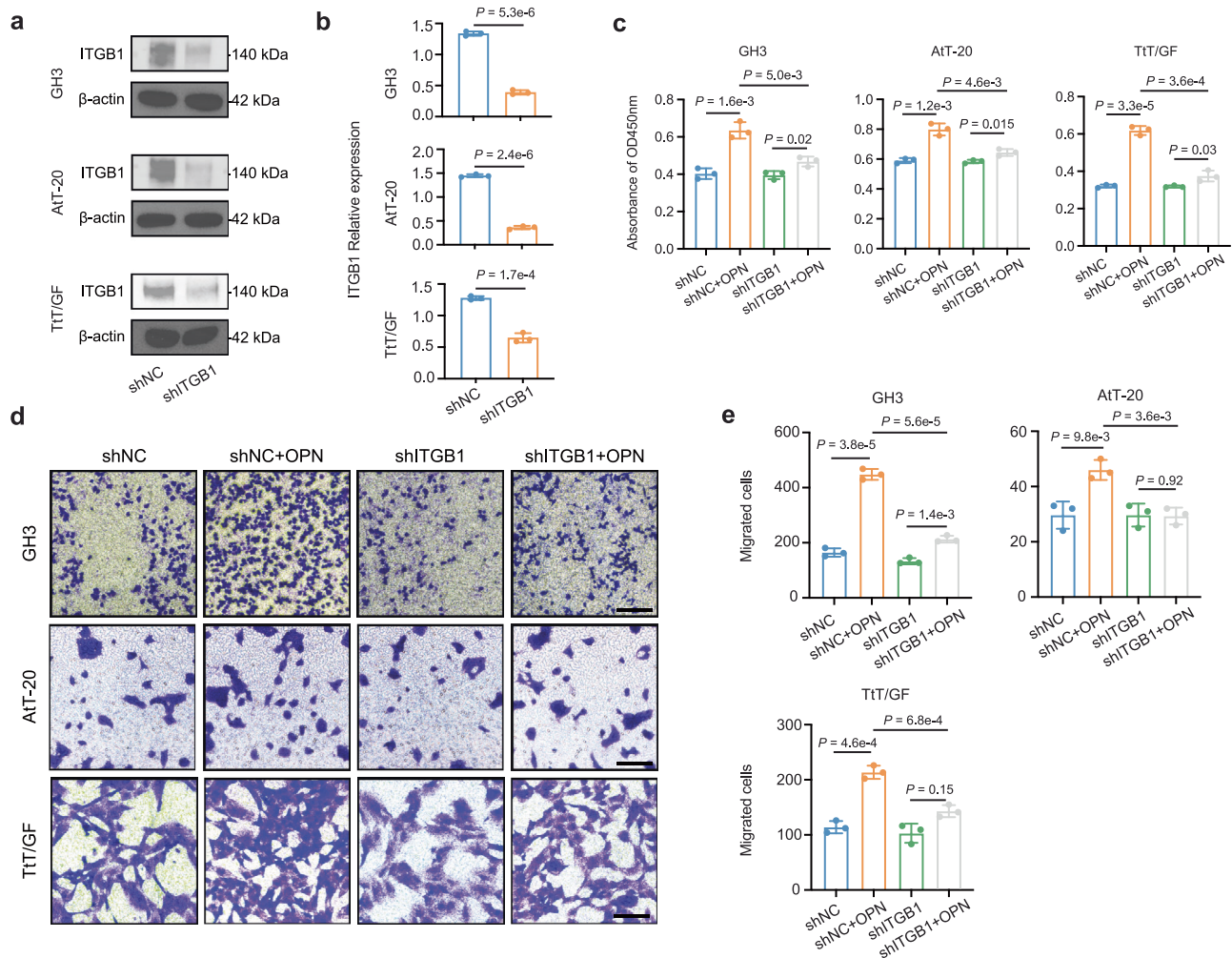


Fig. 8 | ITGB1 knockdown inhibits osteopontin (OPN)-induced proliferation and invasion in pituitary tumor cells. **a** Western blot analysis of ITGB1 expression in GH3, AtT-20, and TtT/GF cell lines. **b** Semi-quantitative analysis of ITGB1 in GH3, AtT-20, and TtT/GF cell lines ($n = 3$ biological replicates). **c** CCK-8 cell viability assay of GH3, AtT-20, and TtT/GF cell lines under specified treatments ($n = 3$ biological replicates). **d** Transwell invasion assay of GH3, AtT-20, and TtT/GF cell lines under

specified treatments ($n = 3$ biological replicates). **e** Quantitative analysis of Transwell invasion assay in GH3, AtT-20, and TtT/GF cell lines under specified treatments ($n = 3$ biological replicates). Scale bar, 100 μ m. Two-sided unpaired t -test was performed for **(b–e)**. Data are presented as mean values \pm SD for **(b–e)**. Source data are provided as a Source Data file for **(a–e)**.

Pathway Enrichment analysis

To quantify the pathway activities within tumor subclusters, we employed the enrichKEGG function from the clusterProfiler package⁶⁷ (version 4.9.2). This function facilitated the retrieval of relevant gene sets from the Kyoto Encyclopedia of Genes and Genomes (KEGG) database. The enrichment significance for each pathway was determined utilizing Fisher's exact test, followed by adjustment of the

p-values using the Benjamini-Hochberg (BH) method to control for false discovery rate.

Developmental Trajectory Inference

To delineate the potential linear differentiation trajectories of tumor cells, we conducted trajectory inference using Monocle2⁶⁸ (version 2.26.0). The process commenced with the construction of a new

CellDataSet object from a Seurat object that had been annotated with cluster information, employing the newCellDataSet function. Subsequently, we utilized the dispersionTable function to identify genes exhibiting significant expression variability, calculating both the mean and dispersion values for each gene. Genes were selected for pseudotime ordering based on a mean expression threshold of at least 0.1 and an empirical dispersion equal to or exceeding the fitted dispersion. Dimensionality reduction was achieved through the application of the DDRTree algorithm, followed by the ordering of cells along the inferred developmental trajectory.

p53 cell cycle-related score calculation

To assess the p53 cell cycle signature within tumor clusters, we referenced gene sets from KEGG. The selection of genes encompassed key cell cycle regulators including *CCND1*, *CCND2*, *CCND3*, *CDK4*, *CDK6*, *CCNE1*, *CCNE2*, *CDK2*, *CCNB1*, *CCNB2*, and *CDK1*. Utilizing the Seurat package, we employed the AddModuleScore function to compute the signature scores specifically within TPIT tumor clusters.

Survival analysis

We conducted a survival analysis by compiling data from patients with pituitary ACTH tumors who underwent surgical intervention at Peking Union Medical College Hospital (PUMCH) between January 2018 and January 2022, with a particular emphasis on patients with tumor recurrence. Tumor specimens were evaluated for p53 immunohistochemical staining (IHC) status and the Ki67 proliferation index. Tumor samples exhibiting positive p53 staining (defined as >10 strongly positive nuclei per 10 high-power fields) and a Ki67 index of 3% or higher were designated as the p53⁺Ki67^{high} group. All other samples were assigned to a separate category. To assess the differential impact on survival, we generated Kaplan-Meier survival curves and determined the statistical significance using the ggsurvplot function from the survminer package (v0.4.9).

Tissue enrichment analysis

For tissue enrichment analysis, we employed the $R_{o/e}$ method as detailed by Zhang et al.^{48,49}. This approach involves calculating the ratio of observed to expected cell counts for specific cell subtype-tissue combinations. Utilizing the R function chisq.test, we determined the observed and expected cell counts, with inputs derived from vectors representing cell type annotations and tissue types. A $R_{o/e}$ ratio exceeding 1 signifies an enrichment of the cell type within the tissue, whereas a ratio below 1 indicates a depletion.

To assess variations in tumor invasion, relapse, and size associated with differing levels of immune stromal cell infiltration, we applied the chisq.test from the stats package (v3.6.2). A p-value threshold of <0.05 was established to define statistical significance.

Spatial transcriptomics sequencing

Pituitary tumor tissues, post-surgical resection, were prepared for spatial transcriptomics by embedding them in optical cutting tissue (OCT) compound and freezing at -80 °C. RNA quality was confirmed using an Agilent 2100, with only samples exceeding an RNA Integrity Number (RIN) of 7 proceeding to spatial gene expression analysis. Cryosections were created and imaged at 20× resolution on a Leica Aperio Versa 8 full slide scanner.

The Visium Spatial Gene Expression Kit (10X Genomics) was employed to construct the sequencing library from a 10 μm tissue section. Each Visium spot has a diameter of 55 μm, capturing transcriptomic data from multiple cells within this spatial resolution. After permeabilization, reverse transcription and library preparation were performed. Sequencing was carried out on the NovaSeq PE150 platform, targeting an average depth of 300 million read pairs per sample.

Spatial transcriptomics data analysis

Raw FASTQ files and histology images were processed using Space Ranger (10X Genomics) with default settings. The resulting gene-spot matrix and aligned image were subjected to further analysis.

Quality control involved the removal of outlier spots with low UMI or Gene counts and spots far away from the main tissue. Seurat (v4.1.0) was used for downstream analysis, including normalization, log-transformation and variable gene selection. PCA was performed, and the first 20 PCs were utilized to construct a graph for UMAP visualization, with batch effects corrected using Harmony. Differential gene expression was assessed using the Wilcoxon algorithm within Seurat, with genes exhibiting $\log_2(\text{fold-change}) > 1$ and an adjusted p-value < 0.05 considered significant. Gene expression patterns were visualized using Seurat's SpatialFeaturePlot function.

Multimodal Intersection Analysis (MIA)

Cell type infiltration within spatial transcriptomics (ST) clusters was inferred through MIA²², comparing the expression levels of cell type-specific genes from scRNA-seq data with area-specific genes from ST data. A lower p-value indicates a greater overlap, suggesting a higher likelihood of cell type presence in the ST niche.

ST spots annotation

To annotate cell types within each spot, we used scRNA-seq-derived cell type marker genes to calculate signature scores for ST data via Seurat's AddModuleScore function. Spearman's correlation analysis was applied to assess the colocalization of cell types within spots based on their signature scores.

Ligand–receptor interaction analysis

CellChat package⁶⁹ (v1.6.1) was utilized to investigate the interactions between cell subtypes within PitNETs TME with default setting by single-cell RNA-seq data. For visualization, we employed the netVisual_bubble function to produce bubble diagrams.

For the spatial transcriptome analysis, we utilized the stLearn package (v4.3.1) to analyze cell-to-cell interactions between neighboring spots. stLearn combined gene expression data from adjacent spots with deep learning-derived features extracted from histopathological images, enhancing the clarity of spatial gene expression. We first loaded established ligand–receptor gene pairs into the stLearn pipeline and then pinpointed spots showing significant interactions between these pairs. For each ligand-receptor pair and each combination of cell types, we recorded the number of instances where the interaction occurred between two specific cell types at adjacent spots. After performing a permutation test on cell type information, we identified interactions with statistical significance ($p < 0.05$). This step allowed us to extract meaningful ligand-receptor pairs from the dataset, providing a focused set of interactions for further analysis.

Immunohistochemistry (IHC) staining

Tissue samples were promptly fixed in a 10% formalin solution for 24 h at room temperature. Post-fixation, tissues were processed into paraffin-embedded blocks, and 4-μm thick sections were prepared using a microtome. Sections underwent deparaffinization and rehydration by successive immersions in xylene twice (20-minute intervals) and a descending series of ethanol baths (100%, 95%, 70% for 5 minutes each), concluding with a rinse in distilled water. Antigen retrieval was executed via heat-induced epitope retrieval (HIER), employing a citrate buffer at pH 6.0 and heated to 100 °C for 10 minutes. To mitigate nonspecific binding, sections were pre-incubated with 5% bovine serum albumin (BSA) in phosphate-buffered saline (PBS) for 1 h. Thereafter, primary antibodies specific for p53 (diluted 1:150) and Ki67 (diluted 1:50) were applied, with incubation continuing overnight at 4 °C. Following extensive PBS washing, sections were treated with their

respective secondary antibodies for 1 h at room temperature. The antigen-antibody complexes were visualized using 3,3'-diaminobenzidine (DAB) as the chromogenic substrate. Sections were then briefly counterstained with hematoxylin for 1 minute, dehydrated through an ethanol and xylene gradient, and mounted with a permanent medium. Each staining run incorporated positive controls (verified p53- and Ki67-positive tissues) and negative controls (omitting primary antibodies) to ensure assay validity.

Bulk RNA-seq validation

The gene expression data for PitNET were retrieved from the Figshare website (https://figshare.com/articles/dataset/Integrated_Proteogenomic_Characterization_across_Major_Histological_Types_of_Pituitary_Neuroendocrine_Tumors/21340161) and GEO database (GSE260487). Utilizing Gene Set Variation Analysis (GSVA), we calculated the signature score for SPP1 for each patient. The resulting score histogram exhibited a bimodal distribution, leading to the stratification of patients into SPP1_{high} and SPP1_{low} groups. We employed the *chisq.test* to assess differences in tumor invasiveness between these two groups.

Fifty hallmark gene sets were obtained from the Molecular Signatures Database (MSigDB, <http://software.broadinstitute.org/gsea/msigdb/>). Subsequently, Gene Set Enrichment Analysis (GSEA, <http://software.broadinstitute.org/gsea/index.jsp>) was conducted to determine the gene signature score for each sample, calculated as the mean scaled expression of all genes within the signatures. The chi-square test was applied to evaluate the significant enrichment of any hallmark gene sets in the SPP1_{high} group, with an FDR-adjusted *p*-value of <0.05 considered indicative of significant enrichment.

A meta-analysis was performed to ascertain the correlation between the SPP1_{high} group and tumor invasiveness. This analysis leveraged the *metabin* function from the *meta* package (v6.5.0), which is specifically designed for the meta-analysis of binary outcomes.

Bulk WES sequencing and data analysis

Genomic DNA from two frozen ACTH tumor tissues was extracted using the Quick-DNA/RNA Microprep Plus Kit (Zymo, D7005) in accordance with the manufacturer's protocol. Sequencing libraries were prepared with Tn5 transposase and subjected to exome capture using TargetSeq® Target Probes (iGeneTech, T600V1), adhering to the provided guidelines. The purified library products underwent quality assessment and were sequenced on the NovaSeq 6000 platform (Illumina) using a 2 × 150 bp paired-end mode, aiming for a minimum coverage depth of 100x to ensure comprehensive data for downstream analysis.

For the bulk exome-seq data, low-quality reads were trimmed using *fastp*. High-quality reads were aligned to the GRCh38 human genome reference using *Bowtie2*. PCR duplicates were identified and flagged using *Picard* tools to minimize artifacts in subsequent analyses. The aligned reads were sorted and indexed with *SAMtools*, resulting in sorted BAM files. Genomic variant call files (gVCFs) were generated using *DeepVariant* (v1.5.0) and subsequently annotated with *ANNOVAR* and *snpEff*.

MAPK and PI3K-AKT pathway score calculation

The gene sets for MAPK and PI3K-AKT pathway were exported using the MSigDB package (version 7.5.1). Utilizing the *Seurat* package, we employed the *AddModuleScore* function to compute signature scores for each pathway in both invasive and non-invasive tumor clusters.

Multiplex immunofluorescence staining

Formalin-fixed, paraffin-embedded (FFPE) human PitNET tissue sections were subjected to multiplex immunofluorescence staining following a sequential staining protocol. The relative markers CD68 (PA014, Abcam, RTU), SPP1 (ab214050, Abcam, 1:2000), αSMA

(19245S, CST, 1:200), ITGAV (AF7308, Beyotime, 1:400), ITGB1 (E-AB-10403, Elabscience, 1:400), FN1 (40932, SAB, 1:300), MYL9 (E-AB-12582, Elabscience, 1:100), ADCYAP1 (FNab10094, FineTest, 1:1500), ANXA1 (AF5114, Beyotime, 1:1000), ASPM (BDPN1665, biodragon, 1:150), BRCA2 (E-AB-40288, Elabscience, 1:1000), CASC5 (PAB31361, bioswamp, 1:1000), PENK (BD-PT5829, biodragon, 1:600), Ki67 (ZM-0166, ZSGB, RTU), tumor markers: ACTH (ZM-0004, ZSGB, RTU), PIT-1 (ZM-0208, ZSGB, RTU), SF1 (GT231702, Genetech, RTU), and TPST (ZM-0318, ZSGB, RTU) were evaluated via IHC. Tissue sections were deparaffinized using an environmental-friendly deparaffinizing solution for 10 min, repeated for a total of three incubations. The slides were then sequentially rehydrated in absolute ethanol (3 min), 95% ethanol (3 min), and 75% ethanol (3 min). Antigen retrieval was performed using an appropriate retrieval solution (PS900(EDTA), abcam) selected based on the primary antibody. The first retrieval was conducted at 100 °C for 20 min, while subsequent retrievals were performed at 95 °C for 30 min. Following antigen retrieval, the slides were washed three times with washing solution. To minimize non-specific binding, tissue sections were incubated with blocking solution (ABT00037, Abcam) at room temperature for 10 min, followed by three washes with washing solution. Primary antibodies were applied to the slides and incubated at 37 °C for 30 min. After incubation, slides were washed three times with washing solution. Fluorescently labeled secondary antibodies (ABT00041, Abcam) were added to the sections, followed by incubation at 37 °C for 30 min. Slides were then washed three times with washing solution. A fluorophore was applied to the slides and incubated at room temperature for 10 min, followed by three washes with washing solution. For multiplex labeling, antigen retrieval and staining steps (steps 2–6) were repeated sequentially for additional targets. After completing staining, sections were mounted with 20 μl of DAPI-containing anti-fade mounting medium (ab104139, Abcam). Coverslips were placed on the slides, and the samples were stored in a dark box until imaging.

To identify SPP1+ TAMs, multi-color fluorescence images were analyzed using HALO Software (version 3.6.4134.396) with the High-Plex FL Module (v4.2.14), focusing on signals from both the SPP1 and CD68 channels. Cell Detection command was performed separately for each channel to ensure accurate identification of SPP1+ and CD68+ cells. For the identification of co-stained SPP1 + CD68+ macrophages, criteria were set to detect cells with overlapping signals from both channels. HALO software automatically quantified the number of positive cells for each marker and the number of co-stained SPP1 + CD68+ macrophages.

Cell culture

Pituitary tumor cell lines AtT-20(ATCC, CRL-1795), GH3(ATCC, CCL-82.1) were cultured in DMEM (ThermoFisher, 11995065) medium supplemented with 10% fetal bovine serum (FBS) (ThermoFisher, 10270106) and 1% penicillin-streptomycin (ThermoFisher, 15070063) under standard conditions of 37 °C in a humidified incubator with 5% CO₂. The pituitary tumor cell line TtT/GF(Procell, CL-0561) is cultured in DMEM/F12 medium supplemented with 10% horse serum, 2.5% FBS, 2 ng/ml basic fibroblast growth factor (bFGF), and 1% penicillin-streptomycin (Procell, CM-0561). Cell lines were authenticated by short tandem repeat (STR) analysis and routinely tested for mycoplasma during experiments, with no contamination detected.

Cell viability assay

Cells were seeded in 96-well plates at an initial density of 3000 cells per well in a final volume of 100 μl. After overnight attachment, cells were treated with either PBS as a control or OPN (Rat OPN protein, MedChemExpress, HY-P79222; Recombinant mouse OPN protein, bioswamp, RPH01180.) at a final concentration of 5 μg/ml. Cell proliferation was assessed using the Cell Counting Kit-8 (CCK-8) (LABEAD, CK001) assay at multiple time points, specifically at 24-, 48-, 72-, 96-, and 120-h

post-treatment. At each time point, 10 μ l of CCK-8 reagent was added to each well and incubated for 1 h at 37 °C. The optical density (OD) was measured at 450 nm using a microplate reader (Agilent Technologies, BioTek Synergy H1) to quantify cell viability. Each experimental condition was performed in triplicate, and background absorbance from blank wells containing medium alone was subtracted from all measurements.

Scratch assay

The scratch assay was performed to evaluate the migratory capacity of TtT/GF pituitary tumor cells in response to mouse OPN treatment. TtT/GF cells were seeded into 6-well plates and allowed to reach ~90% confluence. A uniform scratch was created in the monolayer using a sterile 200 μ l pipette tip, ensuring a consistent width across wells. The wells were gently washed with PBS to remove detached cells and debris. Cells were then treated with PBS or mouse OPN at final concentrations of 1 μ g/ml and 5 μ g/ml, respectively, prepared in serum-free DMEM. The plates were incubated for 24 h under standard culture conditions. Cell migration into the scratch area was documented using an inverted microscope (Nikon, ECLIPSE Ti2-A) at 0- and 24 h time points. Images were analyzed using ImageJ software, and the percentage of wound closure was calculated based on the initial and final scratch widths. Experiments were performed in triplicate, and results were expressed as mean \pm standard deviation. Statistical analysis was conducted using Graphpad Prism 8.0, with significance set at $p < 0.05$.

Transwell assay for pituitary cell lines

The pituitary cell lines TtT/GF, GH3, and AtT-20 were used to evaluate the effects of OPN on cell invasion using transwell invasion assays. Before the assay, cells were treated with PBS or recombinant OPN at concentrations of 1 or 5 μ g/ml for 24 h. Following treatment, the cells were seeded into the upper chamber of a transwell insert (8 μ m pore size, Corning, CLS3422) pre-coated with matrigel (Servicebio, G4131-5ML). The lower chamber was filled with complete culture medium. The cells were then incubated for 24 h at 37 °C in a 5% CO₂ humidified incubator. After incubation, non-invaded cells on the upper surface of the matrigel-coated membrane were carefully removed with a cotton swab, while the invaded cells on the lower surface were fixed with 4% paraformaldehyde. Invasion was visualized by crystal violet staining, and the stained cells were counted under a light microscope (Nikon, ECLIPSE Ni-U) in three random fields per membrane.

Transwell assay for human primary pituitary tumor cells

Fresh tumor tissue samples were collected from two patients diagnosed with pituitary tumors. To obtain single-cell suspensions, the tissue was first minced into small pieces using sterile surgical scissors and transferred to 15 ml conical tubes. The tissue was then incubated with 2 ml of collagenase IV (1 mg/ml, Solarbio, C8160) and DNase I (0.1 mg/ml, Solarbio, D8071) in a shaking incubator at 37 °C for 30 minutes. After incubation, the tissue was mechanically dissociated using a sterile pipette to ensure the complete breakdown of the extracellular matrix. The resulting cell suspension was filtered through a 70 μ m cell strainer to remove any remaining tissue clumps. The cells were then centrifuged at 300 g for 5 minutes and resuspended in serum-free medium. The cells were counted using a hemocytometer, and the viability was assessed by trypan blue exclusion, ensuring a viability rate of over 90%.

Prior to the transwell invasion assay, the cells were treated with PBS or recombinant human OPN (Novoprotein, C544) at concentrations of 1 and 5 μ g/ml for 24 h. The treated cells were then plated onto the upper chamber of a transwell insert pre-coated with matrigel. The lower chamber was filled with complete medium. The cells were incubated for 24 h at 37 °C in a 5% CO₂ humidified incubator. After incubation, non-invaded cells on the upper surface of the matrigel-

coated membrane were carefully removed using a cotton swab, while the invaded cells on the lower surface were fixed with 4% paraformaldehyde. Crystal violet staining was performed to visualize the invaded cells, which were then counted under a light microscope (Nikon, ECLIPSE Ni-U) in three random fields per membrane.

Human pituitary tumor organoid culture

Two fresh pituitary tumor specimens (both silent gonadotroph adenomas) were collected from patients undergoing endoscopic transphenoidal surgery at Peking Union Medical College Hospital (PUMCH). All diagnoses were confirmed through standard clinical, biochemical, and pathological evaluation. Immediately following surgery, the resected tumor tissues were transported on ice to the laboratory, where they were washed three times with sterile PBS. The tissues were then minced into 0.5–1 mm³ fragments using a sterile surgical scalpel in ~1 ml of PBS.

Tumor tissue was first preserved in tissue preservation solution and then immersed in 10 ml PBS containing 10% penicillin-streptomycin for 15 minutes. A digestion solution was prepared using DMEM, 0.5% bovine serum albumin (BSA), 0.35% collagenase (1 mg/ml, Solarbio, C8160), and 0.1% hyaluronidase (1 mg/ml, Solarbio, H8030). The tumor tissue was cut into 1 mm³ pieces, placed in the digestion solution, and shaken at 37 °C, 60 rpm for 15 minutes. After settling, the supernatant was collected in a rinsed centrifuge tube. The supernatant was centrifuged at 4 °C, 300 g for 5 minutes, and the resulting pellet was resuspended in 8 ml erythrocyte lysate and incubated at room temperature for 10 minutes. Following a second centrifugation at 4 °C, 300 g for 5 minutes, the pellet was washed with 8 ml DMEM + 1% penicillin-streptomycin. After another centrifugation, the pellet was resuspended in matrigel (R&D Systems, 3533-010-02), mixed well, and seeded into a 6-well plate (200 μ l per well). The plate was incubated for 20 minutes to allow gel solidification, and 2 ml of complete medium was added to each well for continued cultivation. The complete medium was prepared using advanced DMEM/F-12 (ThermoFisher, 12634010) and supplemented with 1 \times B27 supplement (Biosharp, BL319A), 1.25 μ M N-acetylcysteine (NAC, Innochem, A30872), 5 ng/ml epidermal growth factor (EGF, HY-P7109), 100 ng/ml insulin-like growth factor 1 (IGF-1, Solarbio, P00049), 100 ng/ml noggin protein (GenScript, Z03380), 10 ng/ml fibroblast growth factor 8 (FGF-8, GenScript, Z02989), 5 μ M Y-27632 dihydrochloride hydrate (Y27632, MACKLIN, Y833107), 5 nM triiodothyronine (T3, Shanghai yuanye Bio-Technology, S24025) and 12.5 nM thyrotropin-releasing hormone (TRH, TargetMol, T7407).

To confirm the retention of pituitary tumor-specific markers in organoids, immunofluorescence staining was performed on organoids cultured in 96-well plates. Organoids were fixed in 4% paraformaldehyde (PFA) for 10–15 minutes. After fixation, wash the organoids three times with PBS. Then, permeabilize the cell membrane by incubating the organoids in 0.1% Triton X-100 in PBS for 10 minutes, followed by three PBS washes. Block non-specific binding by incubating the organoids in 10% bovine serum albumin (BSA) for 1 h at room temperature. After blocking, incubate the organoids with the primary antibody (SF1 (GT231702, Genetech), FSH (MXB, MAB-0782), Synaptophysin (ZM-0246, ZSGB-BIO)) overnight at 4 °C. Following primary antibody incubation, wash the organoids three times with PBS and then incubate with the secondary antibody (Proteintech, SA00013-2) for 1 h at room temperature, protected from light. After washing off the secondary antibody, counterstain the organoids with DAPI (Solarbio, C0060), followed by a final PBS wash. Finally, use a confocal fluorescence microscope (Nikon, A1R) to capture images and evaluate positive cells.

Cell viability assay for human pituitary tumor organoid

To evaluate the effect of OPN on organoid viability, organoids were cultured in 96-well plates and treated with either PBS or 5 μ g/ml OPN

for a duration of 15 days. Each well was seeded with $\sim 10 \mu\text{l}$ of organoid-containing matrix gel, ensuring uniform distribution across the plate. The treatment medium was replenished every 3–4 days. After the 15 day incubation period at 37°C with 5% CO_2 , the viability of the organoids was assessed using the CellTiter-Glo Luminescent Cell Viability Assay (Promega, G7570). For this, $100 \mu\text{l}$ of CellTiter-Glo reagent was added to each well containing organoids. The reagent was mixed gently by shaking the plate for 2 minutes to ensure uniform distribution. After 10 minutes of incubation at room temperature to allow for maximal luminescent signal, the luminescence was measured using a microplate reader. Each set of experiments was repeated three times. Subsequently, Ki67 immunofluorescence staining was performed using the Ki67 antibody (ZM-0166, ZSGB-BIO) to further evaluate cell proliferation.

Plasmid construction

Lentiviral vectors encoding short hairpin RNA (shRNA) targeting the ITGB1 gene were designed for specific cell lines: GH3 (ITGB1 shRNA sequence: AATGCCAAATCTTGTGGAGAA), AtT-20 and TtT/GF (ITGB1 shRNA sequence: CCAACCTGTTTACAAGGAATT). A non-targeting shRNA (TTCTCCGAACGTGTCACGT) served as a negative control. The shRNA sequences were synthesized and cloned into the GV493 vector (hU6-MCS-CBh-gcGFP-IRES-puromycin) using AgeI and EcoRI restriction sites. The recombinant constructs were verified by DNA sequencing. All plasmids were obtained from Shanghai Genechem Co., Ltd.

Lentivirus production

The viral vector was transfected into 293 T cells using Lipofectamine 2000 (Invitrogen, Thermo Fisher Scientific, Inc.) along with two helper plasmids, psPAX2 and pMD2.G. Seventy-two hours post-transfection, the lentiviral particles were collected, centrifuged to remove cellular debris, and filtered through $0.45 \mu\text{m}$ cellulose acetate membranes. The viral titer was quantified via fluorescence-activated cell sorting (FACS) based on GFP-positive 293 T cells, yielding $\sim 3.2 \times 10^8$ transducing units (TU)/ml for AtT-20 and TtT/GF cells and 6.5×10^8 TU/ml for GH3 cells. The purified lentivirus was then stored at -80°C for subsequent experiments.

Establishment of ITGB1 Knockdown Cell Lines

To establish ITGB1 knockdown (shITGB1) and control (shNC) cell lines in AtT-20, GH3, and TtT/GF cells, lentivirus carrying ITGB1-targeting shRNA (shITGB1) or non-targeting control shRNA (shNC) was used for transduction. Cells were seeded in six-well plates and infected with lentivirus. After 24 h, the medium was replaced, and cells were cultured for 48 h before selection with puromycin ($4 \mu\text{g}/\text{ml}$, MCE, HY-K1057) for 1 week to establish stable cell lines. Knockdown efficiency was confirmed by western blot to assess ITGB1 protein levels.

Western blot

To assess ITGB1 knockdown efficiency by Western blot, AtT-20, GH3, and TtT/GF cells were lysed using RIPA buffer (Beyotime, P0013B) supplemented with protease and phosphatase inhibitors on ice for 30 minutes, followed by centrifugation at $12,000 \times g$ for 15 minutes at 4°C to collect the supernatant. Protein concentration was measured using a BCA assay (Beyotime, P0011). Equal amounts of protein ($20 \mu\text{g}$) were mixed with $5\times$ SDS loading buffer, boiled at 95°C for 5 min, and separated by SDS-PAGE on a 10% polyacrylamide gel. Proteins were transferred onto a PVDF membrane, which was blocked with 5% BSA in TBST for 1 h at room temperature. The membrane was incubated overnight at 4°C with primary antibodies against ITGB1 (1:1000, abcam, ab179471) and β -actin (1:5000, proteintech, 20536-1-AP) as a loading control. After washing with TBST, the membrane was incubated with HRP-conjugated secondary antibodies (1:5000) for 1 h at

room temperature. Bands were visualized using an enhanced chemiluminescence (ECL) detection system (Bio-Rad, Chemidoc Touch), and semi-quantification analysis was performed using ImageJ software to quantify ITGB1 expression relative to β -actin expression.

Cell viability assay of ITGB1 knockdown cell lines

Cells were seeded in 96-well plates at an initial density of 3,000 cells per well in a final volume of $100 \mu\text{l}$. After overnight attachment, cells were divided into four groups: (1) shNC group: cells transduced with non-targeting control shRNA (shNC) and cultured in normal medium; (2) shNC + OPN group: shNC cells treated with $5 \mu\text{g}/\text{ml}$ OPN; (3) shITGB1 group: cells transduced with ITGB1-targeting shRNA (shITGB1) and cultured in normal medium; (4) shITGB1 + OPN group: shITGB1 cells treated with $5 \mu\text{g}/\text{ml}$ OPN. Cells were cultured for 72 h, and cell proliferation was assessed using the CCK-8 assay at 72 h post-treatment. At each time point, $10 \mu\text{l}$ of CCK-8 reagent was added to each well and incubated for 1 h at 37°C . The optical density (OD) was measured at 450 nm using a microplate reader (Agilent Technologies, BioTek Synergy H1) to quantify cell viability. Each experimental condition was performed in triplicate, and background absorbance from blank wells containing medium alone was subtracted from all measurements.

Transwell assay of ITGB1 knockdown cell lines

The pituitary cell lines TtT/GF, GH3, and AtT-20 were used to evaluate the effects of ITGB1 knockdown and OPN treatment on cell invasion using transwell invasion assays. Before the assay, cells were divided into four groups: shNC, shNC + $5 \mu\text{g}/\text{ml}$ OPN, shITGB1, and shITGB1 + $5 \mu\text{g}/\text{ml}$ OPN. Following 24 h of treatment, the cells were seeded into the upper chamber of a transwell insert ($8 \mu\text{m}$ pore size, Corning) pre-coated with matrigel. The lower chamber was filled with complete culture medium. The cells were then incubated for 24 h at 37°C in a 5% CO_2 humidified incubator. After incubation, non-invaded cells on the upper surface of the matrigel-coated membrane were carefully removed with a cotton swab, while the invaded cells on the lower surface were fixed with 4% paraformaldehyde. Invasion was visualized by crystal violet staining, and the stained cells were counted under a light microscope (Nikon, ECLIPSE Ni-U) in three random fields per membrane.

Statistics and reproducibility

The wilcox.test function, kruskal.test function, chisq.test function in R (v.4.3.1) and GraphPad Prism 8.0 were used to perform statistical testing. The Benjamini-Hochberg method was used to adjust p-values for multiple testing. No statistical method was used to predetermine sample size. No data were excluded from the analysis, except for the scRNA and spatial transcriptomics data points that did not meet the criteria for minimum number of UMIs or genes. The experiments were not randomized. The investigators were not blinded to allocation during experiments and outcome assessment.

Reporting summary

Further information on research design is available in the Nature Portfolio Reporting Summary linked to this article.

Data availability

The public PitNETs bulk sequencing data included in this paper are available in the National Center for Biotechnology Information's Gene Expression Omnibus under accession code GSE260487 (<https://www.ncbi.nlm.nih.gov/geo/>)⁵⁰, and Figshare website (<https://figshare.com/>)⁵¹. The public PitNETs scRNA-seq data were acquired from NCBI BioSample database with BioSample accessions of SAMN18316925, SAMN18316926, SAMN18316927, SAMN18316928, SAMN18316929 (<https://www.ncbi.nlm.nih.gov/biosample/>)²⁰, and National Genomics Data Center (NGDC) under the accession number PRJCA009690

(<https://bigd.big.ac.cn/>)¹⁷ upon request from authors. The raw scRNA-seq and spatial transcriptomics data generated in this study have been deposited at the National Genomics Data Center (NGDC) under the accession number HRA009040 (<http://bigd.big.ac.cn/gsa-human/>). Since these data are related to human genetic resources, raw data access requests will be processed within 3 months by following the guidelines for Genome Sequence Archive for noncommercial use. Data access will be granted for 1 year. All other data supporting the findings of this study have been provided as supplementary tables and source datafiles. Source data are provided with this paper.

References

- Melmed, S. Pituitary-tumor endocrinopathies. *N. Engl. J. Med.* **382**, 937–950 (2020).
- Mete, O. & Lopes, M. B. Overview of the 2017 WHO classification of pituitary tumors. *Endocr. Pathol.* **28**, 228–243 (2017).
- Tritos, N. A. & Miller, K. K. Diagnosis and management of pituitary adenomas: a review. *JAMA* **329**, 1386–1398 (2023).
- Molitch, M. E. Diagnosis and treatment of pituitary adenomas: a review. *JAMA* **317**, 516–524 (2017).
- Petersenn, S. et al. Diagnosis and management of prolactin-secreting pituitary adenomas: a pituitary society international consensus statement. *Nature reviews. Endocrinology* **19**, 722–740 (2023).
- Remba-Shapiro, I. & Nachtigall, L. B. Treatment of acromegaly with oral octreotide. *Best. Pract. Res. Clin. Endocrinol. Metab.* **38**, 101888 (2024).
- Zhong, J. et al. Risk factor analysis and prediction model to establish recurrence or progression of non-functioning pituitary adenomas in men after transnasal sphenoidal surgery. *Sci. Rep.* **14**, 21607 (2024).
- Scheithauer, B. W., Kovacs, K. T., Laws, E. R. Jr & Randall, R. V. Pathology of invasive pituitary tumors with special reference to functional classification. *J. Neurosurg.* **65**, 733–744 (1986).
- Burman, P., Casar-Borota, O., Perez-Rivas, L. G. & Dekkers, O. M. Aggressive pituitary tumors and pituitary carcinomas: from pathology to treatment. *J. Clin. Endocrinol. Metab.* **108**, 1585–1601 (2023).
- Zhang, A. et al. Lactate-induced M2 polarization of tumor-associated macrophages promotes the invasion of pituitary adenoma by secreting CCL17. *Theranostics* **11**, 3839–3852 (2021).
- Wu, X. et al. Single-cell transcriptomics identify a novel macrophage population associated with bone invasion in pituitary neuroendocrine tumors. *J. Exp. Clin. Cancer Res.* **44**, 27 (2025).
- Principe, M. et al. Immune landscape of pituitary tumors reveals association between macrophages and gonadotroph tumor invasion. *J. Clin. Endocrinol. Metab.* **105**, dgaa520 (2020).
- Marques, P. et al. Pituitary tumour fibroblast-derived cytokines influence tumour aggressiveness. *Endocr. Relat. Cancer* **26**, 853–865 (2019).
- Jiang, Q. et al. Tumor-associated fibroblast-derived exosomal circDennd1b promotes pituitary adenoma progression by modulating the miR-145-5p/ONECUT2 axis and activating the MAPK pathway. *Cancers* **15**, 3375 (2023).
- Cornelius, A. et al. Endothelial expression of endocan is strongly associated with tumor progression in pituitary adenoma. *Brain Pathol.* **22**, 757–764 (2012).
- Zhang, D. et al. Single-cell RNA sequencing in silent corticotroph tumors confirms impaired POMC processing and provides new insights into their invasive behavior. *Eur. J. Endocrinol.* **187**, 49–64 (2022).
- Zhang, Q. et al. Single-cell sequencing identifies differentiation-related markers for molecular classification and recurrence prediction of PitNET. *Cell Rep. Med.* **4**, 100934 (2023).
- Lyu, L. et al. Single-cell sequencing of PIT1-positive pituitary adenoma highlights the pro-tumour microenvironment mediated by IFN- γ -induced tumour-associated fibroblasts remodelling. *Br. J. Cancer* **128**, 1117–1133 (2023).
- Yan, N. et al. Single-cell transcriptomic analysis reveals tumor cell heterogeneity and immune microenvironment features of pituitary neuroendocrine tumors. *Genome Med.* **16**, 2 (2024).
- Zhang, D. et al. A human ACTH-secreting corticotroph tumoroid model: novel human ACTH-secreting tumor cell in vitro model. *EBioMedicine* **66**, 103294 (2021).
- Waltman, L. & Jan van Eck, N. A smart local moving algorithm for large-scale modularity-based community detection. *Eur. Phys. J. B* **86**, 471 (2013).
- Moncada, R. et al. Integrating microarray-based spatial transcriptomics and single-cell RNA-seq reveals tissue architecture in pancreatic ductal adenocarcinomas. *Nat. Biotechnol.* **38**, 333–342 (2020).
- Korsunsky, I. et al. Fast, sensitive and accurate integration of single-cell data with harmony. *Nat. Methods* **16**, 1289–1296 (2019).
- Mariotto, A., Pavlova, O., Park, H. S., Huber, M. & Hohl, D. HOPX: The unusual homeodomain-containing protein. *J. Invest. Dermatol.* **136**, 905–911 (2016).
- Yang, Y. et al. PLCG2 can exist in eccDNA and contribute to the metastasis of non-small cell lung cancer by regulating mitochondrial respiration. *Cell Death Dis.* **14**, 257 (2023).
- Li, H. et al. TC2N: A novel vital oncogene or tumor suppressor gene in cancers. *Front. Immunol.* **12**, 764749 (2021).
- Xiao, D. et al. ANXA1 promotes tumor immune evasion by binding PARP1 and upregulating stat3-induced expression of PD-L1 in multiple cancers. *Cancer Immunol. Res.* **11**, 1367–1383 (2023).
- Andrew, M. et al. PAPP2 as a therapeutic modulator of IGF-I bioavailability: in vivo and in vitro evidence. *J. Endocr. Soc.* **2**, 646–656 (2018).
- Perez-Rivas, L. G. et al. TP53 mutations in functional corticotroph tumors are linked to invasion and worse clinical outcome. *Acta Neuropathol. Commun.* **10**, 139 (2022).
- Feng, R. et al. Mutant p53 activates hnRNP2B1-AGAP1-mediated exosome formation to promote esophageal squamous cell carcinoma progression. *Cancer Lett.* **562**, 216154 (2023).
- Ma, H. et al. PBK correlates with prognosis, immune escape and drug response in LUAD. *Sci. Rep.* **13**, 20452 (2023).
- Wright, K. D. et al. The p52 isoform of SHC1 is a key driver of breast cancer initiation. *Breast Cancer Res. BCR* **21**, 74 (2019).
- Hua, H., Kong, Q., Yin, J., Zhang, J. & Jiang, Y. Insulin-like growth factor receptor signaling in tumorigenesis and drug resistance: a challenge for cancer therapy. *J. Hematol. Oncol.* **13**, 64 (2020).
- Kooistra, M. R., Dubé, N. & Bos, J. L. Rap1: a key regulator in cell-cell junction formation. *J. cell Sci.* **120**, 17–22 (2007).
- Zhang, S. et al. Single-cell transcriptomics identifies divergent developmental lineage trajectories during human pituitary development. *Nat. Commun.* **11**, 5275 (2020).
- Karvas, R. M. et al. Use of a human embryonic stem cell model to discover GABRP, WFDC2, VTCN1 and ACTC1 as markers of early first trimester human trophoblast. *Mol. Hum. Reprod.* **26**, 425–440 (2020).
- Walker, M. et al. An NFIX-mediated regulatory network governs the balance of hematopoietic stem and progenitor cells during hematopoiesis. *Blood Adv.* **7**, 4677–4689 (2023).
- Waters, J. A., Urbano, I., Robinson, M. & House, C. D. Insulin-like growth factor binding protein 5: diverse roles in cancer. *Front. Oncol.* **12**, 1052457 (2022).
- Ye, P. et al. TESC associated with poor prognosis enhances cancer stemness and migratory properties in liver cancer. *Clin. Exp. Med.* **24**, 206 (2024).
- Xu, H. et al. Single-cell transcriptome analysis reveals intratumoral heterogeneity in lung adenocarcinoma. *Environ. Toxicol.* **39**, 1847–1857 (2024).

41. Crouch, E. E., Joseph, T., Marsan, E. & Huang, E. J. Disentangling brain vasculature in neurogenesis and neurodegeneration using single-cell transcriptomics. *Trends Neurosci.* **46**, 551–565 (2023).
42. Schupp, J. C. et al. Integrated single-cell Atlas of endothelial cells of the human lung. *Circulation* **144**, 286–302 (2021).
43. Luo, H. et al. Pan-cancer single-cell analysis reveals the heterogeneity and plasticity of cancer-associated fibroblasts in the tumor microenvironment. *Nat. Commun.* **13**, 6619 (2022).
44. Silvín, A. et al. Dual ontogeny of disease-associated microglia and disease inflammatory macrophages in aging and neurodegeneration. *Immunity* **55**, 1448–1465.e1446 (2022).
45. Nalio Ramos, R. et al. Tissue-resident FOLR2(+) macrophages associate with CD8(+) T cell infiltration in human breast cancer. *Cell* **185**, 1189–1207.e1125 (2022).
46. Kohli, K., Pillarisetty, V. G. & Kim, T. S. Key chemokines direct migration of immune cells in solid tumors. *Cancer Gene Ther.* **29**, 10–21 (2022).
47. Tan, J. et al. CCL20/CCR6 axis mediates macrophages to promote proliferation and migration of ESCs by blocking autophagic flux in endometriosis. *Stem Cell Res. Ther.* **13**, 294 (2022).
48. Zhang, L. et al. Lineage tracking reveals dynamic relationships of T cells in colorectal cancer. *Nature* **564**, 268–272 (2018).
49. Guo, X. et al. Global characterization of T cells in non-small-cell lung cancer by single-cell sequencing. *Nat. Med.* **24**, 978–985 (2018).
50. Zhang, Y. et al. Identification of HSPD1 as a novel invasive biomarker associated with mitophagy in pituitary adenomas. *Transl. Oncol.* **41**, 101886 (2024).
51. Zhang, F. et al. Integrated proteogenomic characterization across major histological types of pituitary neuroendocrine tumors. *Cell Res.* **32**, 1047–1067 (2022).
52. Raverot, G. et al. Aggressive pituitary tumours and pituitary carcinomas. *Nat. Rev. Endocrinol.* **17**, 671–684 (2021).
53. Ma, Z. Y. et al. Recurrent gain-of-function USP8 mutations in Cushing's disease. *Cell Res.* **25**, 306–317 (2015).
54. Jung, H. et al. Associations of GNAS mutations with surgical outcomes in patients with growth hormone-secreting pituitary adenoma. *Endocrinol. Metab.* **36**, 342–350 (2021).
55. Tuominen, I. et al. AIP inactivation leads to pituitary tumorigenesis through defective Gai-cAMP signaling. *Oncogene* **34**, 1174–1184 (2015).
56. Lai, Z. Y., Tsai, K. Y., Chang, S. J. & Chuang, Y. J. Gain-of-Function mutant TP53 R248Q overexpressed in epithelial ovarian carcinoma alters AKT-dependent regulation of intercellular trafficking in responses to EGFR/MDM2 inhibitor. *Int. J. Mol. Sci.* **22**, 8784 (2021).
57. Freed-Pastor, W. A. & Prives, C. Mutant p53: one name, many proteins. *Genes Dev.* **26**, 1268–1286 (2012).
58. Sumislawski, P. et al. ACTH-secreting pituitary carcinoma with TP53, NF1, ATRX and PTEN mutations case report and review of the literature. *Endocrine* **76**, 228–236 (2022).
59. Peugeot, S., Zhou, X. & Selivanova, G. Translating p53-based therapies for cancer into the clinic. *Nat. Rev. Cancer* **24**, 192–215 (2024).
60. de Visser, K. E. & Joyce, J. A. The evolving tumor microenvironment: From cancer initiation to metastatic outgrowth. *Cancer Cell* **41**, 374–403 (2023).
61. Tang, W. et al. Revealing the role of SPP1(+) macrophages in glioma prognosis and therapeutic targeting by investigating tumor-associated macrophage landscape in grade 2 and 3 gliomas. *Cell Biosci.* **14**, 37 (2024).
62. Bill, R. et al. CXCL9:SPP1 macrophage polarity identifies a network of cellular programs that control human cancers. *Science* **381**, 515–524 (2023).
63. Fan, G. et al. Single-cell and spatial analyses revealed the co-location of cancer stem cells and SPP1+ macrophage in hypoxic region that determines the poor prognosis in hepatocellular carcinoma. *NPJ Precis. Oncol.* **8**, 75 (2024).
64. Erdogan, B. et al. Cancer-associated fibroblasts promote directional cancer cell migration by aligning fibronectin. *J. Cell Biol.* **216**, 3799–3816 (2017).
65. Elango, J. et al. The molecular interaction of collagen with cell receptors for biological function. *Polymers* **14**, 876 (2022).
66. Xue, R. et al. Liver tumour immune microenvironment subtypes and neutrophil heterogeneity. *Nature* **612**, 141–147 (2022).
67. Yu, G., Wang, L. G., Han, Y. & He, Q. Y. clusterProfiler: an R package for comparing biological themes among gene clusters. *OMICS* **16**, 284–287 (2012).
68. Qiu, X. et al. Single-cell mRNA quantification and differential analysis with Censur. *Nat. Methods* **14**, 309–315 (2017).
69. Jin, S. et al. Inference and analysis of cell-cell communication using CellChat. *Nat. Commun.* **12**, 1088 (2021).

Acknowledgements

The authors thank Dr. Yunfei Zhao of Nanjing Agricultural University for assistance with statistical and coding analysis, Tengwen Zhang from Public Laboratory Platform, National Science and Technology Key Infrastructure on Translational Medicine in Peking Union Medical College Hospital, Yang Yang and Dan Guo from Clinical Biobank in Peking Union Medical College Hospital for experiment assistance. This work was supported by grants from National key research & development plan of China, major project of prevention and treatment for common diseases 2022YFC2505300, subproject: 2022YFC2505304 (L.L.), National High Level Hospital Clinical Research Funding 2022-PUMCH-B-114 (Y.Y.), Chinese Natural Science Foundation 82270405 (X.H.), National S&T Major Project 2023ZD0520400 (C.Z.), and Clinical Medicine Plus X-Young Scholars Project of Peking University, the Fundamental Research Funds for the Central Universities (C.Z.).

Author contributions

Conceptualization and design: L.L., C.Z., H.Z., Y.Y. and X.H. Administrative support: L.L. and Y.Y. Provision of study materials: K.D., Y.Zhang. and Y.Y. Collection of specimens: W.S., Jifang.L. and Jinghua.L. In vitro Experiments: Z.Y. Multiplex Immunofluorescence Staining: Z.Z. and S.Z. Pathological examination: Y.X. and Q.L. Clinical diagnosis and follow-up: Y.Zhao., B.H., H.Y. and F.F. Data analysis and interpretation: C.Z., W.S., L.D., S.C., L.W., F.G., Y.G., W.F. and X.H. Manuscript writing, W.S., C.Z., Y.Y. and L.L. All authors read and approved the final version of the manuscript.

Competing interests

The authors declare no competing interests.

Additional information

Supplementary information The online version contains supplementary material available at <https://doi.org/10.1038/s41467-025-60028-5>.

Correspondence and requests for materials should be addressed to Xiaomin Hu, Yong Yao, Chunhong Zheng or Lin Lu.

Peer review information *Nature Communications* thanks Ryusaku Matsumoto, and the other, anonymous, reviewer(s) for their contribution to the peer review of this work. A peer review file is available.

Reprints and permissions information is available at <http://www.nature.com/reprints>

Publisher's note Springer Nature remains neutral with regard to jurisdictional claims in published maps and institutional affiliations.

Open Access This article is licensed under a Creative Commons Attribution-NonCommercial-NoDerivatives 4.0 International License, which permits any non-commercial use, sharing, distribution and reproduction in any medium or format, as long as you give appropriate credit to the original author(s) and the source, provide a link to the Creative Commons licence, and indicate if you modified the licensed material. You do not have permission under this licence to share adapted material derived from this article or parts of it. The images or other third party material in this article are included in the article's Creative Commons licence, unless indicated otherwise in a credit line to the material. If material is not included in the article's Creative Commons licence and your intended use is not permitted by statutory regulation or exceeds the permitted use, you will need to obtain permission directly from the copyright holder. To view a copy of this licence, visit <http://creativecommons.org/licenses/by-nc-nd/4.0/>.

© The Author(s) 2025

¹Key Laboratory of Endocrinology of National Health Commission, Department of Endocrinology, Peking Union Medical College Hospital, Chinese Academy of Medical Sciences & Peking Union Medical College, Beijing, China. ²Department of Neurosurgery, Peking Union Medical College Hospital, Chinese Academy of Medical Sciences & Peking Union Medical College, Beijing, China. ³Department of Radiology, Peking Union Medical College Hospital, Chinese Academy of Medical Sciences & Peking Union Medical College, Beijing, China. ⁴Department of Pathology, Peking Union Medical College Hospital, Chinese Academy of Medical Sciences & Peking Union Medical College, Beijing, China. ⁵Department of Immunology, School of Basic Medical Sciences, Peking University, Beijing, China. ⁶State Key Laboratory of Molecular Oncology, Beijing Key Laboratory of Cell & Gene Therapy for Solid Tumor, Peking University Cancer Hospital & Institute, Beijing, China. ⁷Frontiers Science Center for Cancer Integrative Omics, Peking University International Cancer Institute, Peking University, Beijing, China. ⁸Clinical Biobank, Peking Union Medical College Hospital, Chinese Academy of Medical Sciences & Peking Union Medical College, Beijing, China. ⁹State Key Laboratory of Complex Severe and Rare Diseases, Peking Union Medical College Hospital, Chinese Academy of Medical Sciences & Peking Union Medical College, Beijing, China. ¹⁰These authors contributed equally: Wan Su, Zhang Ye, Jifang Liu. ✉ e-mail: huxiaomin@pumch.cn; yaoyong@pumch.cn; chunhong_zheng@bjmu.edu.cn; lulin@pumch.cn